Analysis of Mesoscale Atmospheric Flows above Mature Deep Convection Using Super Rapid Scan Geostationary Satellite Data

JASON M. APKE AND JOHN R. MECIKALSKI

Department of Atmospheric Sciences, University of Alabama in Huntsville, Huntsville, Alabama

CHRISTOPHER P. JEWETT

Earth Systems Science Center, University of Alabama in Huntsville, Huntsville, Alabama

(Manuscript received 9 September 2015, in final form 11 May 2016)

ABSTRACT

Super Rapid Scan Operations for the Geostationary Operational Environmental Satellite (GOES) R series (SRSOR) using *GOES-14* have made experimentation with 1-min time-step data possible prior to the launch of the new satellite. A mesoscale atmospheric motion vector (mAMV) program is utilized in SRSOR with a Barnes analysis to produce objectively analyzed flow fields at the cloud tops of deep convection. Two nonsupercell and four supercell storm cases are analyzed. Data from the SRSOR mAMV analysis are compared with both multi-Doppler analyses when available and idealized convection cases within the Weather Research and Forecasting (WRF) Model framework. It is found that using SRSOR data provides several additional trackable targets to produce mAMVs in rapidly ''bubbling'' regions at the deep convective cloud-top level not previously available at lower temporal resolutions (<1 min). Results also show that supercell storm cases produce long-lived maxima in SRSOR cloud-top divergence (CTD) and ''couplet'' signatures in cloud-top vorticity (CTV), which when compared with idealized WRF Model simulations appear to form as a result of environmental horizontal vorticity tilting. Nonsupercell convection in contrast produced weaker, short-lived CTD signatures and no ''CTV couplet'' signatures. These case study results suggest that with SRSOR data it might be possible to uniquely identify supercells using only mAMV-derived flow fields.

1. Introduction

The upcoming launch of the Geostationary Operational Environmental Satellite-R series (GOES-R) platform Advanced Baseline Imager will allow for scanning rates as high as 30 s. Analysis is under way on the current generation of GOES (*GOES-14*) to test the value of high-scanning-rate (<5 min) information in a variety of weather situations (Schmit et al. 2015). In preparation for GOES-R, the *GOES-14* Super Rapid Scan Operations for GOES-R (SRSOR) offers samples of 1-min time-step data over unique meteorological phenomena, including deep convection. The present study began with the visual analysis of a supercell storm over central Colorado on 20 May 2014 that produced a signature not previously observed by satellite scientists when apparent rotation was seen *at the cloud top* in SRSOR observations (Fig. 1; W. Feltz 2014, personal communication). Following the subjective, observational analysis, the question was raised as to whether this rotation signature on 20 May 2014 could in fact be the mesocyclone with the convective system as resolved by radar and discussed in Browning (1964), Lemon and Doswell (1979), and Weisman and Klemp (1982, 1984) in supercell thunderstorms.

While Rabin et al. (2004) looked at near-convective-environment satellite-derived motion over convection using *GOES-12* imagery for mesoscale convective systems; no prior attempt has been made to quantify mesoscale satellite-observed motion fields on the convective storm scale using the SRSOR high-scanning-rate data from *GOES-14*, as suggested by Schmit et al. (2015). Aside from the benefit of having storm-scale flow data outside regions covered by extensive radar networks, objective identification of convective cloud-top outflow by GOES data could yield new methods for identifying and quantifying the updraft strength in storms at high temporal resolution without the need for multi-Doppler radar data. Cloud-top outflow

Corresponding author address: Jason Apke, University of Alabama in Huntsville, 320 Sparkman Dr., Huntsville, AL 35805. E-mail: jason.apke@gmail.com

DOI: 10.1175/JAMC-D-15-0253.1

© 2016 American Meteorological Society

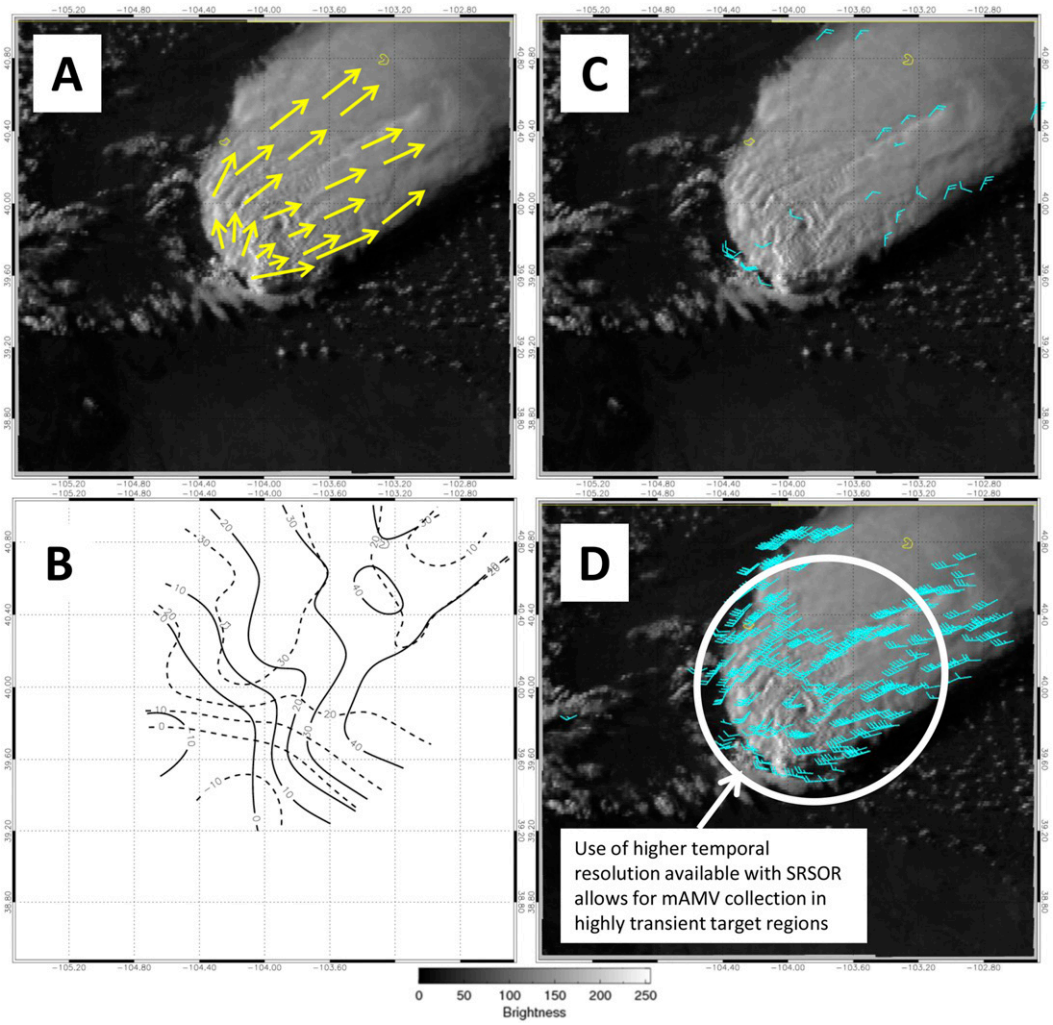

FIG. 1. The 2337 UTC 20 May 2014 example of mAMVs over a supercell in central Colorado with (a) subjective flow observations from tracking SRSOR visible data targets; wind vectors are scaled based on observed target motion. (b) Single-pass Barnes analysis of u (solid) and v (dashed) vector magnitudes (m s^{-1}). (c) Current 7-min GOES rapid scan mAMVs as compared with (d) 1-min *GOES-14* super rapid scan–derived mAMVs with GOES visible imagery.

has already proven useful with 5-min single-Doppler radar data for forecasting hail size (e.g., Witt and Nelson 1991). Identification of updraft strength with time and particular cloud-top flow patterns unique to severe weather occurrences could also prove useful for satellite and ground-measurement-based severe weather nowcasting algorithms such as the Probability of Severe Convection algorithm (ProbSevere; Cintineo et al. 2014), the Thunderstorm Strike Probability Nowcasting Algorithm (THESPA; Dance et al. 2010), and the Global/Regional Assimilation and Prediction System–Severe Weather Forecast Tool (GRAPES–SWIFT; Hu et al. 2007; Wilson et al. 2010).

In this paper we examine six convective cases with a simple objective analysis method of SRSOR, so-called mesoscale atmospheric motion vectors (mAMVs; Bedka and Mecikalski 2005; Bedka et al. 2009), to quantify what is subjectively observed in super rapid scan data. Sections 2 and 3 describe the background and methodology, including how the mAMVs are derived, a description of the objective analysis method used, a synopsis of the cases, and a brief description of supplemental experimentation involving the use of multi-Doppler radar data and a cloud-resolving model experiment to validate observed mAMV flow fields. Sections 4 and 5 discuss the results and conclude the paper, respectively.

2. Background

Fujita (1968) and Hubert and Whitney (1971) introduced some of the first known objective techniques

for measuring atmospheric motion vectors (AMVs) using imagery from geostationary satellites. In simple terms, AMVs are derived from the motion of clouds using infrared (IR), water vapor, and visible satellite imagery. Operational GOES AMV techniques (Velden et al. 1997, 1998) are focused on deriving wind vectors that are accurately height assigned and close to the background geostrophic wind such that they can be used by many data assimilation centers to improve the initial conditions of numerical weather prediction (NWP) models, especially in data-sparse regions within the GOES field of view (~55°S–~55°N; Velden et al. 1997; Bedka et al. 2009). AMVs are routinely derived from all geostationary satellites, including Meteosat satellites and *Himawari-8*.

AMV-derived winds at the cloud-top level have been used for the purposes of analyzing hurricane dynamics and subsequently improving NWP model forecasts. Specifically, finer temporal resolution of target-tracking-based AMVs substantially increased the wind information measured for Hurricane Luis in 1995 (Velden et al. 2005). Overall, the 5-min time-step data provided cloud-top information on slowly evolving areas near and around the hurricane eyewall. Areas of convective storm initiation have also been explored by identifying upper-level divergence with satellite AMVs, as in the work of Rabin et al. (2004), who found that while the spatial resolution of water-vapor-derived AMV divergence fields was lower than that available from the Rapid Update Cycle NWP model, they provided valuable observational data for preconvective triggers where surface boundaries may be weak.

As a means of extending the AMV methods toward identifying nongeostrophically balanced flows, mAMVs were developed and are currently used in the near-operational *GOES-R* convection initiation (CI) algorithm (Mecikalski and Bedka 2006; Walker et al. 2012; Mecikalski et al. 2015). The mAMVs are formed using the same algorithms as operational AMVs, yet the constraints to a background NWP model wind field are reduced. With lower constraints to the background wind field, AMVs that describe more of the storm- and meso-β-scale (20–200 km) winds are retrieved than are otherwise available with operational algorithms. As a specific example, within the GOES-R 0–1-h CI algorithm, convective cloud object tracking is used with mAMVs to estimate future cumulus cloud locations such that a spatial overlap comparison of cloud objects in the next 7–15-min image time frame can be made (Walker et al. 2012). The mAMVs have been shown to help track the prerainfall state of growing cumulus clouds with reliable skill, thereby allowing one to forecast deep convection with Lagrangian cloud-top brightness temperature changes using GOES data alone (Mecikalski and Bedka 2006; Mecikalski et al. 2008; Walker et al. 2012).

Supercell flow dynamics are commonly studied through the use of ground-based radar information (e.g., Browning 1964, 1965; Marwitz 1972; Brandes 1977, 1978, 1981, 1984a,b; Brandes et al. 1988). More recent studies of supercell dynamics involve examinations of finescale radar data from mobile measurements and fixed dual-polarization platforms (Bluestein et al. 1995, 2010; Wurman et al. 1997; Biggerstaff et al. 2005; Kumjian and Ryzhkov 2008; French et al. 2014). The dynamics of supercell and nonsupercell storms are comprehensively reviewed in Klemp (1987) and Davies-Jones et al. (2001). The generation of vertical vorticity in a vertically sheared environment can be understood using the storm-relative, linearized vertical vorticity equation, neglecting Coriolis force:

$$\left(\frac{\partial \zeta'}{\partial t}\right)_{\mathrm{sr}} = -(\overline{\mathbf{v}} - \mathbf{c}) \cdot \nabla_h \zeta' + \overline{\mathbf{S}} \times \nabla_h w' \cdot \hat{\mathbf{k}}, \qquad (1)$$

where the Eulerian vertical vorticity perturbation (ζ') change with respect to time is a function of storm-relative advection by the mean wind $\overline{\mathbf{v}}$ and storm motion $\mathbf{c}$ vectors, as well as vorticity tilting, which is a term comprising the mean shear vector (defined as $\overline{\mathbf{S}} = d\overline{\mathbf{v}}/dz$), vertical velocity perturbation w', vertical unit vector $\hat{\mathbf{k}}$, and the horizontal gradient operator ∇_h. The vertical velocity can also be related to horizontal divergence with integration of the anelastic mass continuity equation (Witt and Nelson 1991). Understanding the horizontal flow characteristics at the cloud top can thus be related back to ongoing supercell processes in deep convection that involve both w' and ζ'.

Few studies have been performed that focus on the analysis of satellite-derived cloud-top motions for the purposes of understanding the dynamics of mature deep convection, which was largely related to the low temporal resolution of GOES relative to radar data (nominally 15 vs 5 min) that limits the ability to resolve motions in rapidly "bubbling" regions at the cloud top (Bedka et al. 2015; Schmit et al. 2015). Deriving divergence information with satellite data in the post-CI mode of convective storms has been achieved at lower temporal resolutions within the ProbSevere product (Cintineo et al. 2014), which uses the Warning Decision Support Services–Integrated Information *w2segmotionll* algorithm (Lakshmanan et al. 2007) combined with postprocessing techniques described in Sieglaff et al. (2013) to grow pixels from a maximum in emissivity based on a combined *k*-means and enhanced watershed technique. The cloud objects are derived on three

different saliency (or aerial extent) scales to identify small, medium, and large objects, which are then postprocessed into a final objectively identified product with time-derived expansion rates (Sieglaff et al. 2013). The cloud-object-derived expansion rates are compared to radar data and environmental values derived by NWP model fields to produce the probability of severe weather occurrence within the next hour (Cintineo et al. 2014). While ProbSevere does successfully link satellite and radar information throughout the entire life cycle of storms, the *w2segmotionll* approach for deriving cloud-top expansion can be sensitive to rapid geometric shifts, merging, and splitting of individual cloud clusters. More recent satellite studies of convection have begun using SRSOR data to analyze rapid changes in overshooting tops and cloud-top cirrus, and these studies have found potential links between overshooting tops and the occurrence of severe weather at the ground (Bedka et al. 2015; Schmit et al. 2015).

Use of 1-min data for AMV flow derivation has typically been avoided because of the navigational problems involved with older satellites in the GOES series (Velden et al. 2005). With advanced altitude and star tracker systems, GOES-O series instruments have improved image navigation and registration over previous geostationary instrument systems (Schmit et al. 2013). This study presents a first look at mAMVs from *GOES-14*-based 1-min SRSOR data, with mitigated navigational issues of the previous models, to analyze mature deep convective dynamics via geostationary satellite data.

3. Methodology

a. The mAMV processing for storm-top analyses

The derivation of AMVs is based on target identification with satellite data. Targets include gradients, minima and maxima across IR brightness temperature T_B, water vapor, and visible reflectance fields. Targets are identified through an eight-point measurement system and tracked through three consecutive satellite images (typically 15 min apart). Target height is determined via comparison of temperature and water vapor channels to NWP datasets; for this study, Global Forecast System (GFS) data are used. Targets and images are quality controlled using a series of multichannel checks to ensure they do not contain multideck images (clouds at multiple heights that are producing gradients) or coastlines. Navigation checks with known coastal locations are also performed to ensure no satellite "wobble" is contaminating the AMV target locations. The direction and speed of the remaining targets at different heights are produced and quality controlled based on an NWP-derived flow field. Typical quality control values of the operational AMVs are tuned to remove motions that deviate from synoptic-scale movements.

The mAMVs are calculated by modifying the GFS NWP background flow requirement and quality control values to allow for more motions that deviate from the mean flow. This study follows the quality index (QI; Holmlund 1998) and recursive filter (RF; Hayden and Purser 1995) score thresholds set by Bedka and Mecikalski (2005) to derive mAMVs. The QI is a designed score to test the consistency of vectors via nearest-neighbor wind coherency checks (Holmlund 1998). For operational data, a high QI value of 60 is required for a vector to be considered in analyses; the mAMV threshold used is 25. Further, the RF score (Hayden and Purser 1995) with operational AMVs, designed to test AMV speed and direction consistency with objectively analyzed GFS NWP data, is lowered from the operational threshold of 0.9 to 0.01. Hence, by lowering the QI and RF score values, we allow vectors to deviate from quasi-gradient wind balanced flow, and observed vectors are not constrained to the GFS NWP output that may not appropriately characterize storm- or mesoscale motions caused by deep convection. The quality of the current experimental mAMVs has been shown to be worse than operational high quality control AMV wind results in comparison to vertical wind profilers (Bedka et al. 2009); however, these were mAMV observations made with 15–30-min satellite data time steps.

Observations of SRSOR-derived mAMVs suggest that without navigational issues introduced by *GOES-8* and *-10* (e.g., Velden et al. 2005), the number of mAMVs increases substantially over deep convection with the higher temporal resolution (Fig. 1). An example mAMV plot over a supercell storm in central Colorado comparing the more traditional 7-min GOES rapid scan mAMVs (Fig. 1c) with 1-min SRSOR *GOES-14*-derived mAMVs (Fig. 1d) demonstrates an ability to derive kinematic flows (Fig. 1b) over storm tops that appear to follow subjective observations (Fig. 1a) with minimal noise, per the retrieval methodology described here. The SRSOR mAMVs are then repurposed in this study for use specifically on the tops of mature convective clouds.

Within the analysis to follow, the main alteration made to the Bedka and Mecikalski (2005) mAMV methodology is that the vertical domain of the allowed vectors was changed to retrieve vectors near the convective equilibrium level, with a lower-level cutoff at approximately 500 hPa and an upper limit of 100 hPa. The relatively low-altitude cutoff, compared to average convective equilibrium levels over the United States, is used to allow vectors in our analysis to be calculated on the entrained, optically thin (visible optical depth

values < 10) edge of the cirrus anvils in cumulonimbus structures. Dry air entrainment and anvil cirrus advection into clear air causes targets to have higher values of T_B. With increased layer material transmissivity, warmer ground-based IR radiation is observed through the cloud. A T_B and NWP model-based AMV height assignment methodology will thus yield lower heights along cirrus platforms that are in reality relatively constant in altitude. Since the vectors calculated at or near the cloud edges are important to understanding flow at the tops of deep convection, they are kept in the analysis by using a deep pressure threshold. A topic of future studies will be to identify vectors that only occur at identified convective cloud tops to improve operational use feasibility.

b. Cloud-top flow field derivation

It is the deep convective cloud-top flow fields that are of interest in the present study, contrary to the traditional AMV operational perspective for a derivation of a total synoptic-scale, quasi-gradient wind balanced vertical wind profile. A key assumption made in this work is that all winds observed are at a relatively constant height (i.e., from a "single level" or "single plane"), which allows for the objective derivation of deep convective cloud-top flow fields that mimic what is subjectively observed. Our analysis has shown that the single-plane assumption has problems in multideck cloud situations, such as along or near cloud edges where the presence of vertical wind shear may affect assumed two-dimensional flow. In contrast, on cloud tops, such as over deep convection, the single-plane assumption produces a smooth flow field that is not sensitive to optical-depth-related height changes assumed in NWP T_B comparison-based derivations. It should be noted that broad overshooting tops with large height differences that deviate from the mean anvil height may cause problems with this single-plane assumption, although the current spatial resolution of mAMVs such as that shown in Fig. 1d and as shown in the upcoming figures likely is too coarse for this to be a significant problem. As the spatial density of vectors increases, future studies may use objective overshooting top identification algorithms such as that discussed in Bedka et al. (2015) for the removal of vectors with excessive height differences to focus only on anvil-level flow.

Once mAMVs were derived from the SRSOR data for storm tops, two flow field characteristics were analyzed: the cloud-top horizontal divergence (CTD; $\nabla_h \cdot \mathbf{V}$), where $\mathbf{V}$ is the velocity vector, and the cloud-top vertical vorticity (CTV), defined as the vertical component of the curl of the velocity vector ($\hat{\mathbf{k}} \cdot \nabla \times \mathbf{V}$) with ∇ representing the three-dimensional gradient operator. The point-source information of mAMVs is converted into a 0.01° × 0.01° latitude–longitude grid using a Barnes objective analysis procedure (Barnes 1964, 1973; Koch et al. 1983) to produce fields of CTD and CTV. Since an objective of this work is to develop a product that requires a computationally inexpensive and fast method for calculating flow fields in an operational setting, tests were performed on a quick Barnes (1973) single-pass method. For the mAMV analysis, equilibrium-level GFS NWP model data are used as background first-guess fields. The first-guess fields are designed to approximate synoptic flows near the equilibrium level. The Barnes analysis takes the first-guess grid data and converges to the observed solutions on the grid, and is not sensitive to the actual background values so long as they are a close approximation of the actual scalar field (Barnes 1964). In this experimental phase, our analysis used 6-h GFS forecast data to simulate real-time implementation, with bilinear interpolation between grid points used to determine the first-guess values for each observation. The background first-guess field was updated every 6 h, consistent with GFS data availability. While GFS NWP data do not capture storm-scale (10–60 km) motions associated with mature deep convection, as discussed in Barnes (1964), the Barnes objective analysis is not very sensitive to changes in the first-guess field and converges quickly on the mAMV-observed solutions with each successive pass.

The Barnes analysis "falloff" and "convergence" parameters were designed to resolve the flow features that were subjectively observed in our preliminary analysis (Fig. 1b), and are calculated using the method outlined in Koch et al. (1983) and described in appendix A. Through experimentation, it is found that despite the increase in mAMV information with SRSOR, flow fields are still sensitive to the addition and subtraction of information as targets change at the cloud top. Problems can arise when using a Barnes analysis over a nonuniform grid, and as such the analysis can "balloon" in areas with large data gaps. The balloon effect is defined in Koch et al. (1983) as large phase and amplitude distortions in the field of grid points that are primarily determined by one nearby observation and is common in highly irregular grids. The balloon effect in data-gap regions was noted to cause rapid geometry and amplitude changes in the CTD field that did not appear to realistically follow the overshooting tops observed with satellite IR T_B data at several times in our case study analysis.

One solution to this balloon effect problem involves the use of a time collection methodology to make a denser mAMV observation field over the storm systems

of interest. To smooth rapid flow changes that occur with the transient detectability of targets at the cloud top, 5 min of data collection were used per flow field calculation to allow for a comprehensive dataset that is not sensitive to rapid mAMV spatial density changes. It is assumed that a given convective storm maintains a quasi-steady state through the 5-min collection period for each frame. During the collection period, 1-min image triplets are used to generate one set of mAMVs. An image triplet is a set of three satellite images, each ~1 min apart in SRSOR, used to derive the mAMVs. The processer moves ahead 1 min, and generates another set of mAMVs with the next set of SRSOR image triplets. This process is repeated for 5 min and is hereafter referred to as time smoothing. Vectors through the 5-min time-smoothing period are advected to a single time frame for objective analysis with 0–6-km GFS-derived storm motion data to account for the horizontal movement of a storm. Thus, every objective analysis flow field uses six (including 0 min) individually derived mAMV fields. For example, an objective analysis at 2005 UTC would use mAMVs derived from 2005 UTC back to 2000 UTC, which are advected from 0 to 5 min forward in time with storm motion, respectively. Using a 5-min time-smoothing period maintained the realistic CTD phenomena that followed IR-observed overshooting tops of deep convection. A further explanation of why flow fields are sensitive to losing mAMV information in particular areas is included in appendix A.

While time smoothing of SRSOR-derived mAMVs has notable sensitivity to non-steady-state storms, improved resolutions in time and space at the launch of GOES-R will mitigate target loss and likely remove the need to use time smoothing all together. It should be noted that the mAMV flow fields derived from *GOES-14* data in this study are thus a simulated version of what GOES-R will be capable of with more routine super rapid scan data involving 30-s time steps (Schmit et al. 2015). With the assumptions made, mAMVs are then used to derive the CTD and CTV gridded fields in order to analyze mature deep convective case studies.

c. Case studies

This study uses SRSOR data for six convective storm events in 2014. Four cases are supercells, identified based on radar data, and two cases are nonsupercell convection. Supercells were defined in a manner consistent with Davies-Jones et al. (2001) as long-lived (>1 h) storms with both severe weather reports and mesocyclones observed with Doppler velocity shear $\geq 6\,\mathrm{m\,s^{-1}}$ and a differential velocity $\geq 30\,\mathrm{m\,s^{-1}}$ over multiple tilts (over a depth of 3 km and at altitudes less than 5 km above the radar level) for multiple radar scans (longer than 5 min). Storm reports (tornado, wind, and hail) were collected from the Storm Prediction Center (SPC) archive online (SPC 2015). Cases were selected specifically to test convective storms with dynamically distinct characteristics, such as distinct updraft "maintenance" mechanisms, and storms were examined in several different convective environments over the United States.

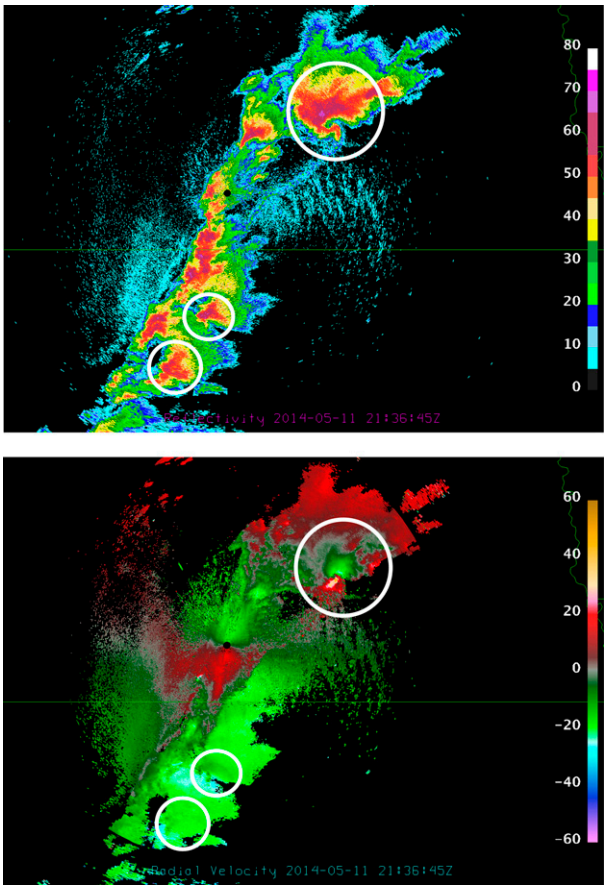

FIG. 2. The 2136 UTC 11 May 2014 KUEX WSR-88D (top) 0.5° tilt reflectivity (dBZ) and (bottom) velocity ($\mathrm{m\,s^{-1}}$) for three identified supercells over the central plains. Supercells with identifiable mesocyclones are highlighted with white circles.

Three storms of interest occurred on 11 May 2014 within the SRSOR domain. The three supercells were analyzed by satellite and radar over central Nebraska and northern Kansas (Fig. 2). The Hastings, Nebraska (KUEX), Weather Surveillance Radar-1988 Doppler (WSR-88D) depicted three identifiable mesocyclones and "hook" echoes with storms that initiated along a dryline. The supercell that developed over central Nebraska produced 19 individual SPC tornado reports. The two convective storms over Kansas produced severe

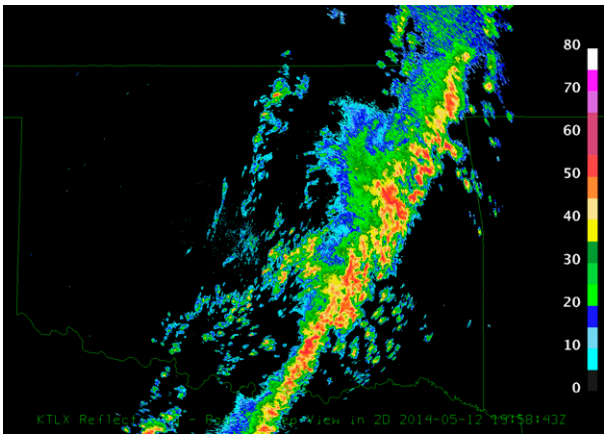

FIG. 3. Radar reflectivity (dBZ) at 1958 UTC 12 May 2014 at Norman (KTLX).

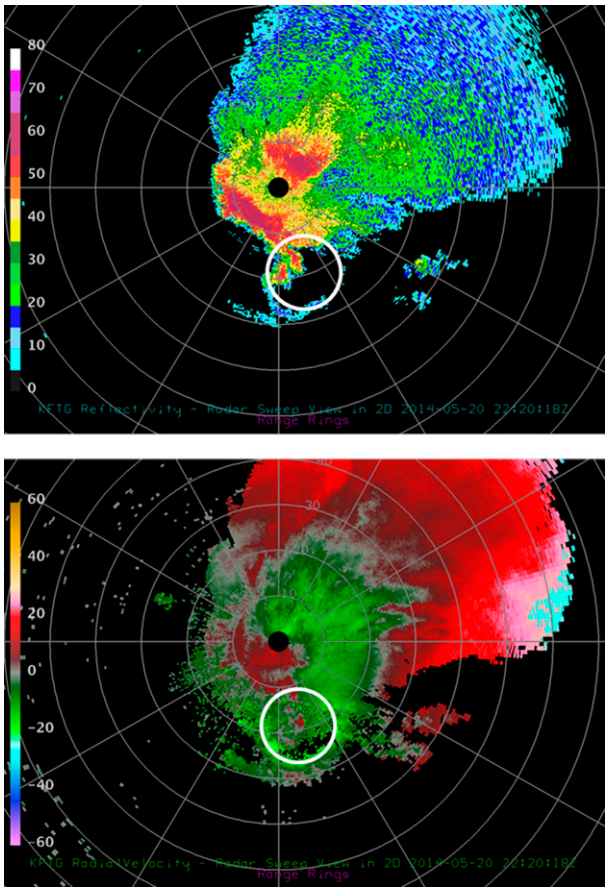

FIG. 4. The 2220 UTC 20 May 2014 (top) 8° tilt reflectivity (dBZ) and (bottom) velocity (m s^{-1}) at Oklahoma City, Oklahoma (KFTG), with a mesocyclone highlighted in the white circle with range rings plotted every 10 km.

hail, with the northern storm producing hail of up to 1.75 in. (1 in. = 2.54 cm) in diameter, and the southern storm producing hail of 1-in. diameter.

On the morning of 12 May 2014 over central Oklahoma, separate storms occurred along a cold front from the same synoptic system involved in the 11 May 2014 case, but without the vertical shear present to allow the cells of interest to develop mesocyclones. Nonsupercell storms initiated south of Norman, Oklahoma, by 1600 UTC. Convective storms initiated along the cold front by 2000 UTC over eastern Oklahoma and eventually evolved into a quasi-linear convective system (QLCS; Fig. 3).

Convective storm events on 20 May and 21 May 2014 included two discrete supercells that gave the initial inspiration to conduct this study. The 20 May 2014 case was a long-lived, discrete supercell over central Colorado (Fig. 4) that initiated at 1955 UTC. This cell initiated in an area with minimal cirrus cloud contamination from the surrounding environment and minimal interference from nearby convection. Therefore, the flow signatures visible from an mAMV standpoint are likely "uncontaminated" in the sense that cirrus cloud motions from non-supercell-related clouds do not produce mAMVs that interfere with the derived CTD and CTV fields, which may be the case in 11 May 2014 and which is discussed further in appendix B. The 21 May 2014 case was another day during which a discrete supercell formed in central Colorado and eventually grew upscale into a nighttime mesoscale convective system (MCS).

Another supercell case study occurred over the eastern United States during an SRSOR data collection effort, where two supercells produced severe hail and tornadoes in western Delaware and eastern Virginia on 22 May 2014. Two supercells initiated on a weak occluded cold front that moved through a strongly heated area with a large upper-level jet maximum (>40 m s^{-1} at 300 hPa). The last case was nonsupercell convection over northern Alabama on 18 August 2014. The nonsupercell convection was well sampled by the Hytop, Alabama (KHTX), WSR-88D and the Huntsville, Alabama, Advanced Radar for Meteorological and Operational Research (ARMOR; Peterson et al. 2005) radar system located at the Huntsville International Airport (34.645°N, 86.771°W), in addition to SRSOR data. Further details of all cases analyzed are provided in section 4.

d. Supplemental experimentation

Two forms of supplemental analysis were performed: multi-Doppler radar analysis and Advanced Research version of the Weather Research and Forecasting Model (ARW; Skamarock et al. 2005) idealized simulations. These radar and ARW modeling analyses were

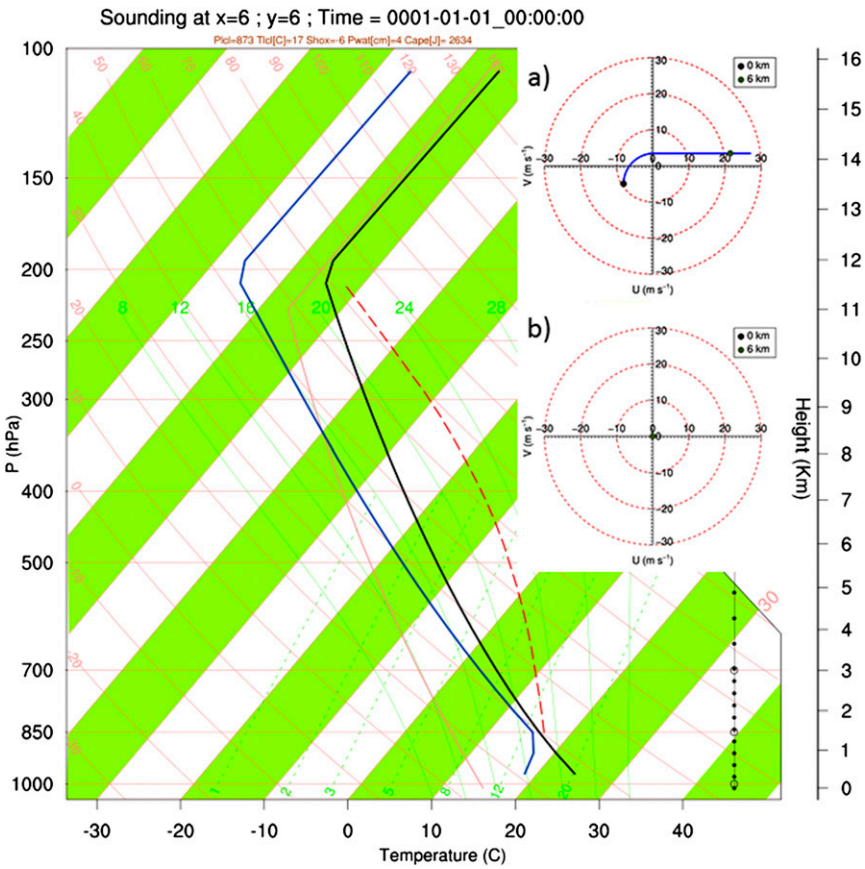

FIG. 5. Initial sounding for the idealized ARW cases with hodographs for (a) the quarter-circle shear case and (b) the 0 m s^{-1} no-mean-wind-with-height case. See text for further description of the WRF Model settings.

performed to address questions brought forth in the mAMV analysis concerning the quality of the measured vectors. Since the kinematic fields in question occur at the cloud top, multi-Doppler analysis only allows for a rough quality check of analyzed cloud-top flow fields using a different measurement system. Multi-Doppler analysis was performed on the 18 August 2014 cells when both radars were able to scan well above a non-supercell thunderstorm. The ARMOR and KHTX radars were converted to a 300 km × 300 km × 15 km Cartesian coordinate system with a 1 km × 1 km × 1 km grid spacing using a Cressman objective analysis scheme (Cressman 1959) and a 1.2-km radius of influence in the NCAR REORDER system (Oye et al. 1995). The Custom Editing and Display of Reduced Information in Cartesian Space (CEDRIC; Mohr et al. 1986) system was then used on the Cartesian grid to return two-dimensional horizontal flow values, which were then input into a downward integration scheme of the mass continuity equation assuming vertical motion $w = 0$ above the storm top at 15 km. Values of corrected horizontal motion were then used to derive divergence near the storm top after application of a three-pass linear least squares two-dimensional filter. Derived radar motion data at high altitudes may contain large errors caused by the high vertical component of the beam direction and underdetermined radar observations of the horizontal wind components: u and v. A comprehensive discussion on the errors associated with dual-Doppler wind retrieval in the upper levels is available in Potvin et al. (2012a,b). The multi-Doppler analysis is thus considered only in the near-storm-top region around 9 km to compare divergence locations with resolved SRSOR CTD locations.

Because of the problems involved with collecting a reliable multi-Doppler sample of the upper levels of a storm, the SRSOR mAMV flow field properties are also explored with a cloud-resolving ARW model simulation. Running an ARW model simulation is prudent given that rapid bubbling convection could potentially violate common assumptions made when calculating mAMVs in that the cloud drift motions may

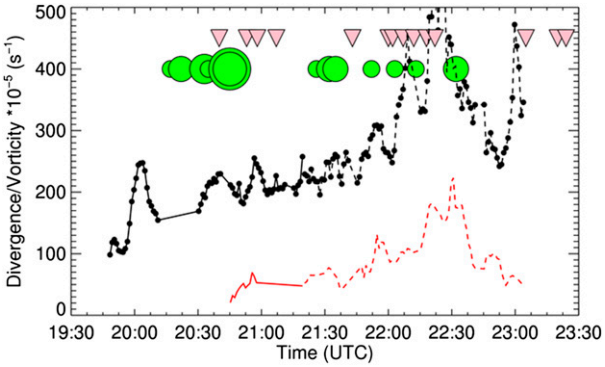

FIG. 6. The 11 May 2014 central Nebraska supercell SRSOR CTD (black) and positive CTV (red) maximum values closest to the overshooting top identified by visible satellite data with SPC tornado reports (pink triangles) and hail reports scaled by size (green circles). The dashed line type represents time frames during which the CTD and CTV maxima occurred in areas with low mAMV spatial density and we suspect these were affected by Barnes analysis "ballooning."

not represent actual horizontal motions of winds. For example, gravity waves may propagate at speeds unrelated to the horizontal wind motions, yet still produce prominent target samples for the Bedka and Mecikalski (2005) mAMV method. Rapid bubbling of deep convection on subsatellite scanning rate time scales may also appear to be horizontal motion, which would fool a horizontal target cross-correlation scheme for flow derivation. Using SRSOR data likely mitigates the latter problem; however, the raised concerns in mAMV quality justify the need to experiment with NWP model results to ensure that observed mAMV flow fields follow understood upper-level deep convective dynamics. The ARW model simulation is also used to test the association of the observed mAMV dynamics with the hypothesized obstacle flow-related dynamics of the enhanced-V signature (Brunner et al. 2007) and the generation mechanism of vertical vorticity at the cloud top for both supercell and nonsupercell thunderstorms. The mechanism of vertical vorticity generation is explored using the nonlinearized vertical vorticity equation, neglecting the effects of the Coriolis force, which is expressed as

$$\frac{D\zeta}{Dt} = \underbrace{-\zeta(\nabla_h \cdot \mathbf{V})}_{\mathrm{A}} \underbrace{-\left(\frac{\partial w}{\partial x}\frac{\partial v}{\partial z} - \frac{\partial w}{\partial y}\frac{\partial u}{\partial z}\right)}_{\mathrm{B}} + \underbrace{\frac{1}{\rho^2}\left(\frac{\partial p}{\partial y}\frac{\partial \rho}{\partial x} - \frac{\partial p}{\partial x}\frac{\partial \rho}{\partial y}\right)}_{\mathrm{C}}. \tag{2}$$

In Eq. (2), the total rate of change with time t of vertical vorticity ζ is a function of vorticity stretching (A), tilting (B), and solenoidal (C) terms on the right-hand side of the equation, where u, v, and w in the tilting term retain their typical definitions as the components of flow in the x, y, and z directions, respectively. The variables p and ρ in the solenoidal term represent pressure and density, respectively.

This ARW version-3.7.1 model simulation experiment used the Weisman and Klemp (1982) characteristic sounding as a horizontally homogeneous environment throughout the 84 km × 84 km × 20 km domain. The vertical domain is set to contain 200 exponential eta-model layers with an approximately constant ~120-m vertical grid spacing. Horizontal grid-point spacing is set to 200 m × 200 m, which is computationally affordable and less than 1 km, as suggested by Bryan et al. (2003), and is consistent with other similar WRF-based supercell studies (e.g., Cintineo and Stensrud 2013; Kumjian et al. 2015). The simulation uses a horizontal fifth- and a vertical third-order positive definite advection scheme. The model also uses the Morrison double-moment microphysical scheme (Morrison et al. 2005). Convection is initiated by inserting a 10 km × 10 km × 1.5 km spheroid warm bubble with a 3-K maximum positive temperature perturbation, and is performed for 60 min with 1.5-s integration time steps to ensure numerical stability. Two wind profiles are examined: one with a quarter-circle hodograph (Fig. 5a) and the other with no mean flow (Fig. 5b), which are part of the available configuration for these simulations in ARW. As we know from Weisman and Klemp (1982), without environmental shear, the zero mean wind with height experiment will produce a three-dimensional flow example of nonsupercell convection. The quarter circle will produce a splitting supercell, with a dominant right-moving storm. Vorticity and divergence will be analyzed in sections 4f and 4g on a three-dimensional scale with a focus on near-cloud-top environments, which will then be compared with observations of SRSOR case studies.

4. Results

a. 11 May 2014: Supercell

CI occurred over central Nebraska, surpassing 35 dBZ of reflectivity at 1942 UTC on 11 May 2014. Maximum CTD and CTV values near the overshooting top tracked subjectively with respect to time show large values of

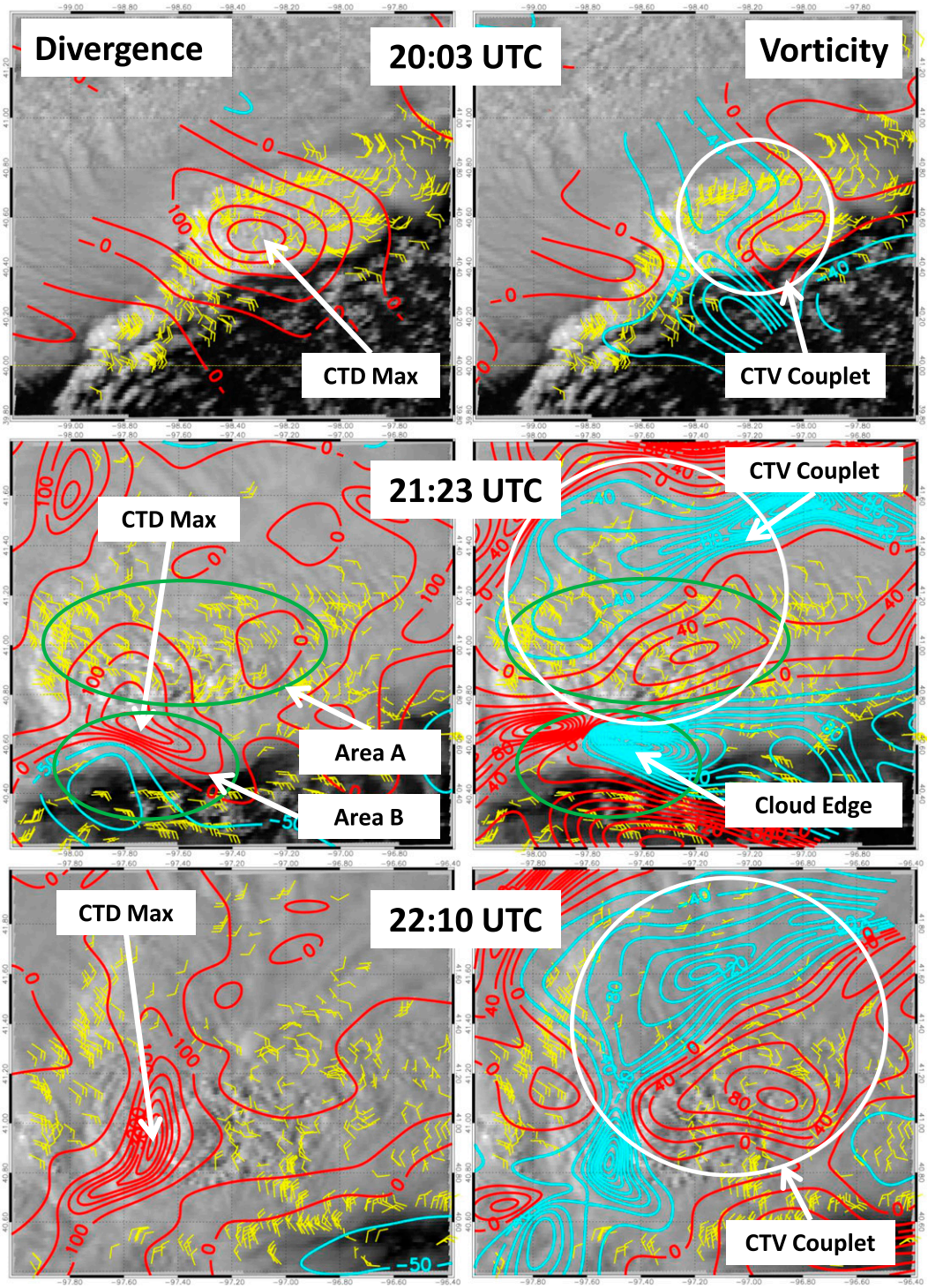

FIG. 7. Selected 11 May 2014 SRSOR GOES visible satellite data with equilibrium-level flow-relative SRSOR mAMVs (m s^{-1}) over central Nebraska and (left) CTD contoured every 50×10^{-5} s^{-1} and (right) CTV contoured every 20×10^{-5} s^{-1} with positive (negative) values for both in red (blue). The green circles are areas referenced in appendix B.

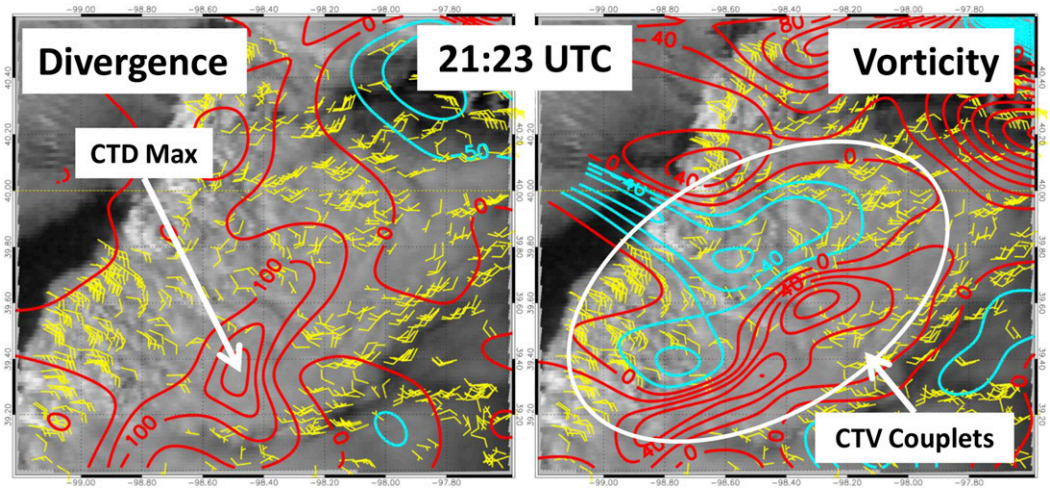

FIG. 8. As in Fig. 7, but over southern Nebraska and northern Kansas.

CTD (>0.001 s^{-1}) by 1949 UTC (Fig. 6). The cell moved directly over the Hastings radar site and exhibited supercell storm characteristics by 2001 UTC, with broad-scale rotation observed around the radar cone of silence. The first indication of a "CTV couplet" (adjacent maxima in vorticity of opposite signs over a storm) was witnessed by 2003 UTC (Fig. 7); however, the positive local CTV maximum disappeared by 2007 UTC and was not observable again until 2040 UTC (not shown). By 1954 UTC, a sharp increase in CTD is observed over a ~10-min period, as values approached 0.0025 s^{-1} by 2003 UTC. The first report of 1-in. hail occurred by 2017 UTC (during a temporary gap in *GOES-14* satellite data). CTD maintained a steady and strong signal > 0.002 s^{-1} between 2034 and 2101 UTC. The first tornado report occurred at 2040 UTC, with several more reports made at 2053, 2058, and 2107 UTC. Both CTD and CTV (the positive and negative CTV) oscillate in magnitude throughout the life span of the supercell. By 2123 UTC, two additional CTV couplet signatures are visible in northern Kansas (Fig. 8). The cyclonic component of the CTV couplet on the Nebraska storm appeared to be in a well-sampled region downstream of the updraft at 2123 UTC in Fig. 7. At 2123 UTC, the CTD maximum shifts south as raw mAMVs near the cloud edge of the Nebraska storm appear to be impacting the pattern of the objectively analyzed flow (see appendix B). Despite the Barnes oversmoothing contamination, observations of raw mAMVs in Fig. 7 near the overshooting top of the system at 2123 UTC show a divergence signal associated with this storm. Several tornado reports occurred at 2210 and 2300 UTC. While large increases in CTD magnitudes and overshooting tops occur after 2210 UTC, along with an increase in tracked CTV, it is notable that the maximum in CTD is occurring in a large data gap and may be enhanced by "ballooning" in the Barnes analysis. The large data gap exceeded 40 km at times after 2210 UTC near the overshooting top and likely resulted in the unrealistic objectively identified increases in CTD magnitude shown in Fig. 6 at this time.

When compared with the Hastings radar dataset, all three of these systems exhibit supercell characteristics, including the presence of mesocyclones and reflectivity "hook" echoes (see Fig. 2). At 2140 UTC the CTV signatures in northern Kansas quickly disappear as the two convective cells appear to merge into a larger system associated with a trailing cold front (not shown). An analysis of radar data suggested that developing convection nearby might have affected the cloud-top flow signatures with the Kansas cells (Fig. 9). By 2230 UTC, anvil motion dynamics from several adjacent storms

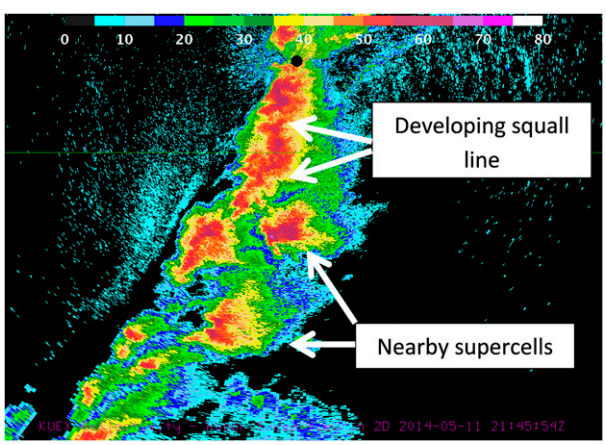

FIG. 9. The 0.5° tilt reflectivity (dBZ) at 2145 UTC 11 May 2014 from the KUEX WSR-88D.

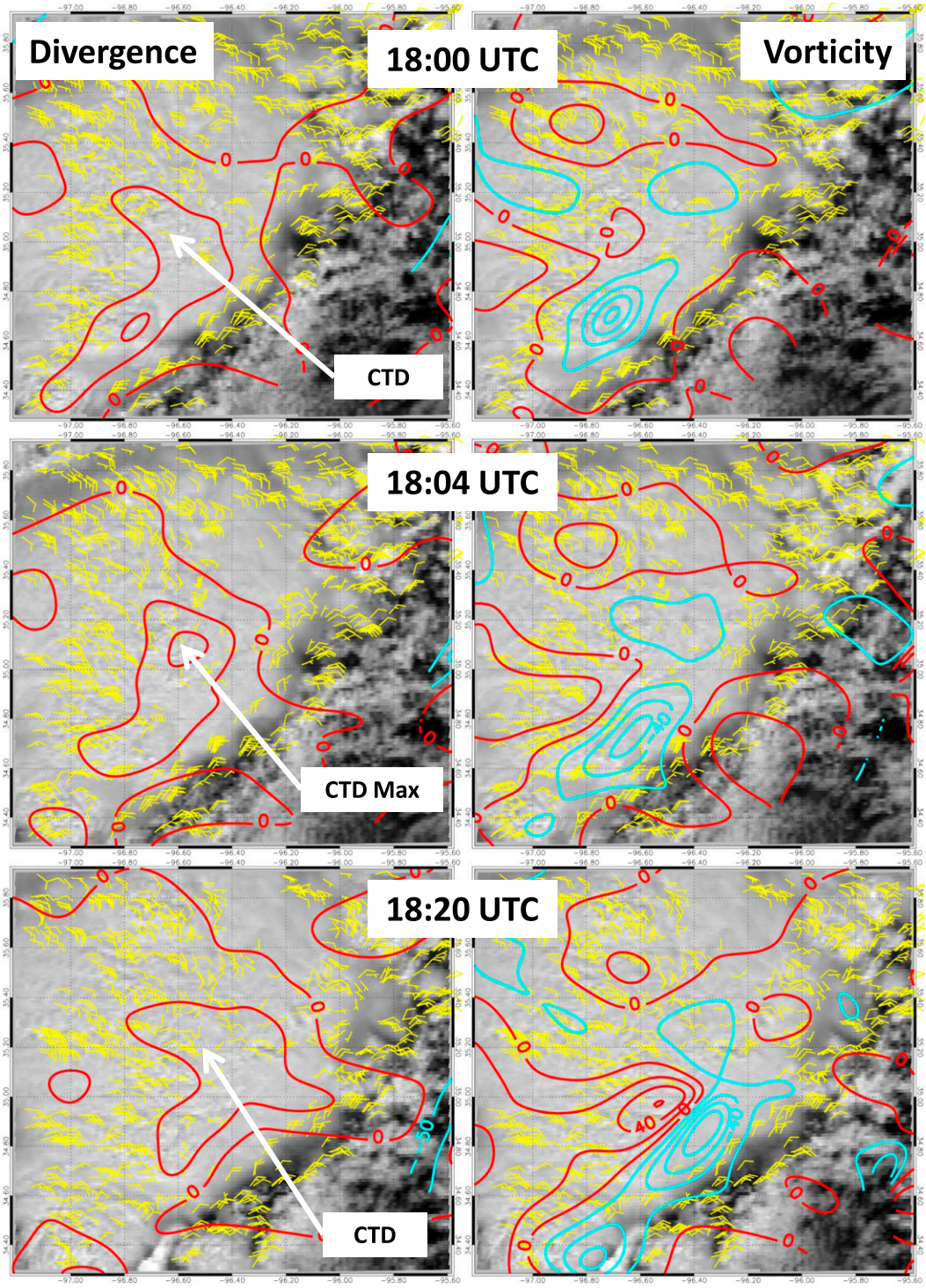

FIG. 10. As in Fig. 7, but for 12 May 2014 over central OK.

along the synoptic boundaries begin to mix with one another, and the CTV couplet signature on the central Nebraska storm becomes less coherent than it was in its quasi-discrete form. Despite anvil coverage, Barnes oversmoothing, and interference from nearby clouds on deriving mAMVs, the CTV couplet signature in central Nebraska remains trackable on the cell until the system grows upscale to an MCS at 2300 UTC.

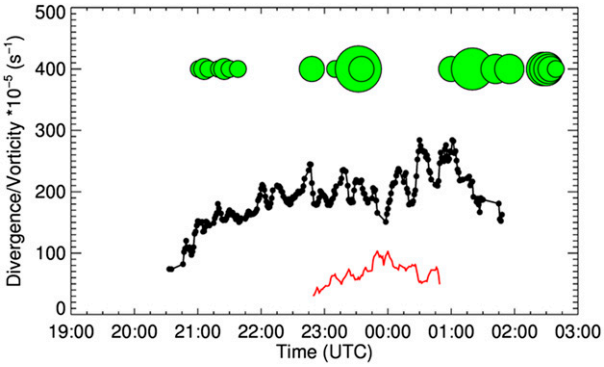

FIG. 11. The 20 May 2014 central Colorado supercell SRSOR CTD (black) and positive CTV (red) maximum values closest to the overshooting top identified by visible satellite data with SPC hail reports scaled by size (green circles).

b. 12 May 2014: Nonsupercell

Deep convection initiated near 1650 UTC on 12 May 2014 during the SRSOR data collection process, with CTD values over central Oklahoma peaking near $7.5 \times 10^{-4}\,s^{-1}$. By 1700 UTC the CTD in a storm cell over southern Oklahoma peaked at values $>0.001\,s^{-1}$. One distinct feature when compared to 11 May 2014 is that nonsupercell convection CTD early on 12 May 2014 (1630–1830 UTC) exhibited highly transient behavior in a storm-relative sense. While large CTD values were observed, local maxima $>0.001\,s^{-1}$ typically did not last longer than 20 min (Fig. 10). After 1903 UTC, CTD resembled a quasi-linear pattern along the line of storms as the systems grew upscale, with values peaking above $0.0015\,s^{-1}$. While CTD was strong ($>0.0015\,s^{-1}$) along the convective line, individual CTD maxima were only maintained for 15–30 min, compared to the long-lived 4-h CTD signature seen on 11 May 2014. Continuous CTV couplet signatures such as those seen on 11 May 2014 are not present in this case throughout the duration of the event.

c. 20 May 2014: Supercell

CI occurred over central Colorado, with CTD values that exceed $7.5 \times 10^{-4}\,s^{-1}$ by 2032 UTC. By 2058 UTC the storm was mature enough to produce CTD $>$ $0.001\,s^{-1}$. A CTD maximum was coherent and trackable near the overshooting top for 6 h from UTC to 0200 UTC when sunset occurred (Fig. 11). After ~2100 UTC, the cell exhibited a quasi-constant CTD near $0.0015\,s^{-1}$. The CTD field intensified by 2200 UTC, and subsequently increased to a maximum of over $0.002\,s^{-1}$ in less than 10 min. A mesocyclone was observed on radar (see Fig. 4) at 2220 UTC. Hail was observed (SPC report) at 2248 UTC with a diameter of 1.5 in. after the CTD increased to $\sim 0.0025\,s^{-1}$ at 2246 UTC. The CTV couplet signature first became apparent by 2300 UTC (Fig. 12). The largest hail report (2.75-in. diameter according to the SPC) occurred at 2332 UTC during a time when CTD values were exceeding $0.002\,s^{-1}$. The discrete nature of the cell made both the CTD and CTV couplet signatures very clear by 2337 UTC when using cloud-top SRSOR mAMVs. Observations of the raw mAMVs that are depicted in the right two columns of Fig. 12 show clear cyclonic rotation juxtaposed with a CTD maximum and a rotation signature without the same information gaps near the present overshooting tops as seen on 11 May 2014. The storm produced additional large-hail reports (ranging from 1.5- to 2.5-in. diameter) after 0100 UTC during a time at which CTD values were peaking near $0.0028\,s^{-1}$. Note that CTD may not have ceased at 0200 UTC but, rather, the version of the mAMV algorithm used for this study requires the visible channel and is presently a daytime-only algorithm.

d. 21 May 2014: Supercell

Discrete convection was visible by satellite at 1853 UTC over central Colorado. No obvious correspondence was visible between the SPC tornado reports and the Barnes objectively analyzed CTD and CTV values upon observation of the time series (Fig. 13). By 1931 UTC the cloud top had expanded enough to produce a CTD maximum with values near the overshooting top at $0.0011\,s^{-1}$. Hail of 1-in. diameter was initially reported to the SPC at 1920 UTC with the storm near Conifer, Colorado. The CTD exhibited an intensification period starting at 1940 UTC with values of $\sim 0.001\,s^{-1}$, and peaked at 2007 UTC to values near $0.0022\,s^{-1}$. After the initial increase in CTD values (and data gap in the *GOES-14* SRSOR sampling), CTD values were observed to be $>0.0035\,s^{-1}$ by 2039 UTC, although the values of the objective analysis appear to be associated with a spatial data gap in mAMV observations and may again have been caused by ballooning in the Barnes objective analysis. A CTV couplet was observed at 1958 UTC (Fig. 14). Because of the less transient nature of the negative CTV maxima compared to the positive maximum value, CTV minima were observed near the overshooting top and were tracked in time for this storm. Local maxima in the CTV couplet signature values were noted to occur 5–7 min after observable maxima in CTD, although larger values of CTD do not appear to correspond to larger values of CTV. Several tornadoes occurring near Denver and Aurora, Colorado, at 2016 and 2030 UTC, were reported by storm spotters. The peak SPC hail report diameter of 1.75 in. occurred at 2239 UTC in Adams County, Colorado. The CTD oscillated around $0.002\,s^{-1}$ throughout the mature lifetime of the system; however, it is notable

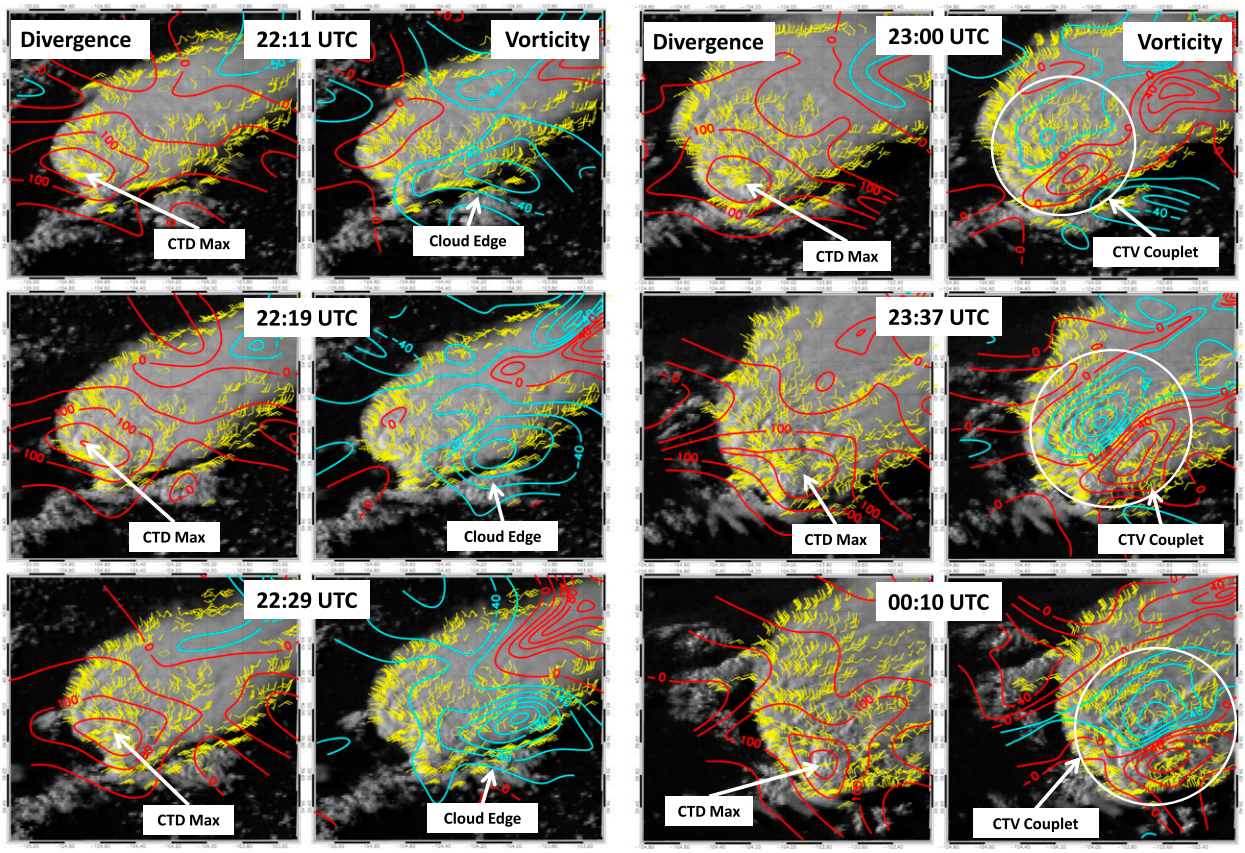

FIG. 12. As in Fig. 7, but for 20 May 2014 over central Colorado.

that a spatial gap in mAMV coverage >40 km near the overshooting top may have again affected the Barnes objective analysis after 2200 UTC for both CTD and CTV. Similar to 11 May 2014, this system exhibited a persistent, strong CTD signature for 4 h, prior to the system eventually growing upscale to an MCS. The CTV couplet signature was observable for 3 h and was no longer observable after 2300 UTC.

e. 22 May 2014: Supercell

Two discrete supercells produced tornadoes in the eastern United States over Delaware and Virginia. While the cell over Delaware was identified by the SRSOR CTD methodology, cirrus contamination from deep convection occurring upstream in southern Pennsylvania may have affected the observable flow patterns. The cirrus over and around the Delaware storm did not appear to be directly associated with the Delaware storm, which suggested that the mAMV measurements came from a different system (Fig. 15 and appendix B). The supercell storm over eastern Virginia remained discrete and uncontaminated by nearby cirrus clouds throughout its life cycle, and was first observable at 1946 UTC. The CTD derived for the Virginia storm was weaker than the cells observed on 11, 20, and 21 May 2014 (Fig. 16). Furthermore, at no point during the lifetime of this cell was there an observable CTV couplet in either the Barnes

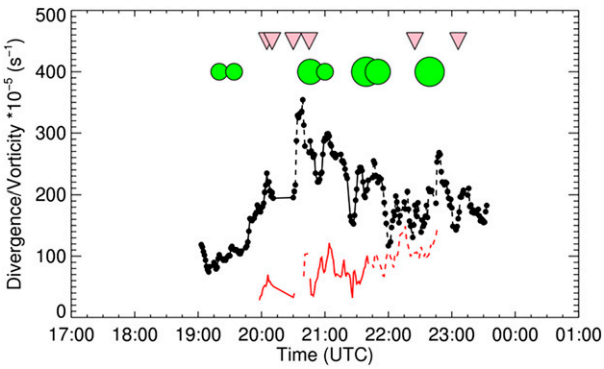

FIG. 13. The 21 May 2014 central Colorado supercell SRSOR CTD (black) and positive CTV (red) maximum values closest to the overshooting top identified by visible satellite data with SPC tornado reports (pink triangles) and hail reports scaled by size (green circles). The dashed line type represents time frames during which the CTD and CTV maxima occurred in areas with low mAMV spatial density and we suspect that they were affected by Barnes analysis ballooning.

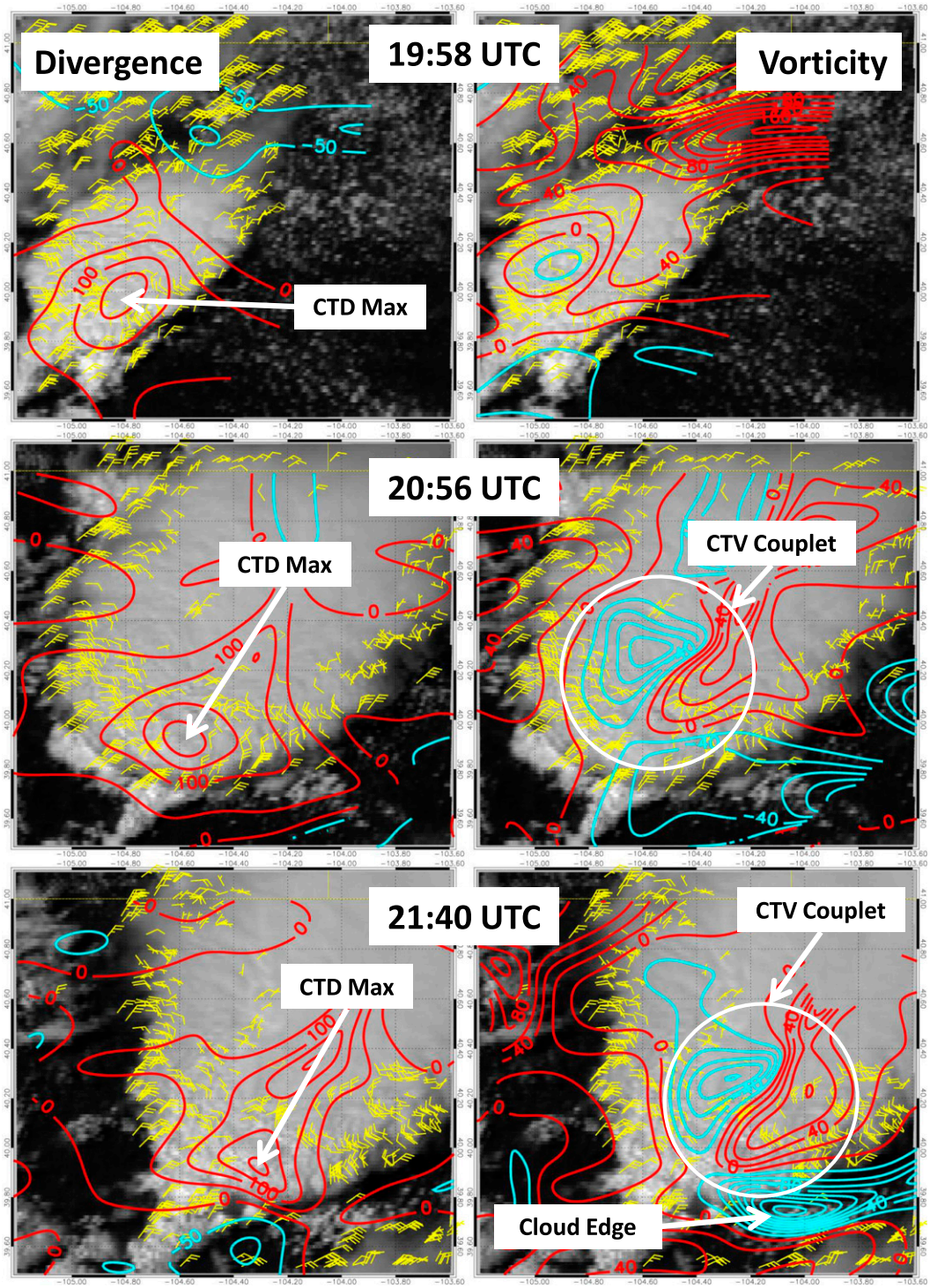

FIG. 14. As in Fig. 12, but for 21 May 2014.

objective analysis or the raw mAMVs (Fig. 17). The storm cell in Delaware also did not produce a notable CTV couplet. Hail was observed to be smaller as compared to the three previous supercell case studies, typically around 1-in. diameter. The CTD values were also lower than for the previous three supercells. CTD values were around $0.001\,s^{-1}$ for the Virginia storm, with a local maximum value at 2141 UTC occurring 4 min

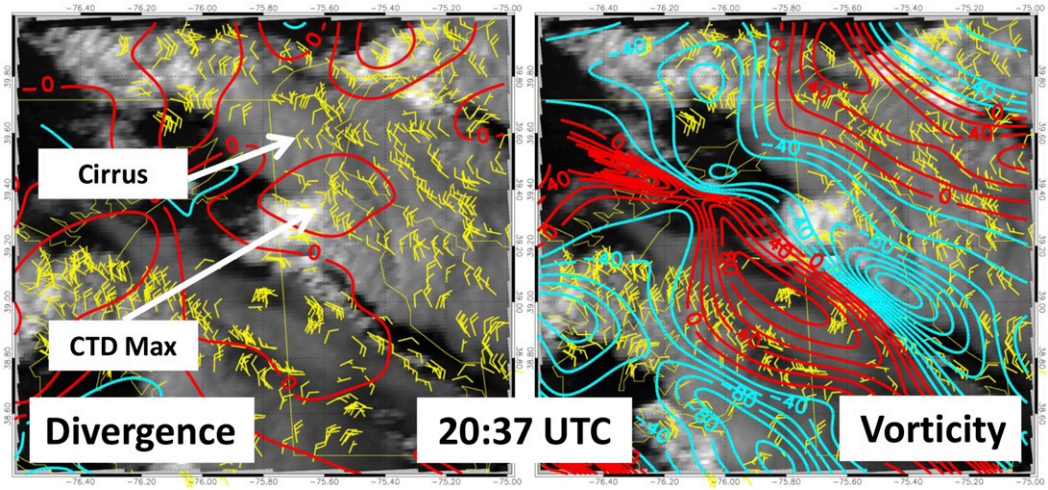

FIG. 15. As in Fig. 7, but for 22 May 2014 over northern Delaware.

before a tornado report in Prince George County, Virginia. By observing SPC-reported hail sizes from all four supercells with the average CTD in a 10-min period prior to the storm report, it is found in our small sample size that a majority of smaller hail reports (~1-in. diameter) occur with CTD values around $0.001\,s^{-1}$ (Fig. 18a). Comparing the average values of CTD and hail size for all four cases shows that the 22 May 2014 case had much lower average hail size and CTD values than did the other three supercells (Fig. 18b). The result that larger hail sizes are coincident with larger CTD values is consistent with the findings of Witt and Nelson (1991) in their analysis using single-Doppler velocities to characterize upper-level storm outflow. A second tornado report occurred in Sussex County, Virginia, at 2220 UTC, with no corresponding CTD maximum, again showing no obvious relationship between the Barnes objective cloud-top flow and SPC tornado reports at the ground. Despite the weaker values of CTD, a maximum for both storms was persistent and simple to track for ~3 h.

f. 18 August 2014: Nonsupercell

Several small nonsupercell convective storms were observed in a low vertical shear environment. Convective cells that did produce CTD signatures $> 5 \times 10^{-4}\,s^{-1}$ were typically observable for 30 min (Fig. 19). Maxima associated with these cells peaked at values much lower than those for the supercell cases, typically near $6 \times 10^{-4}\,s^{-1}$. These cells were below severe limits, with only one SPC wind report occurring in Marshall County, Alabama, at 2120 UTC. No cells in this case study produced CTV couplets like those observed in three of the supercell cases. The proximity of several of these storms to the KHTX and ARMOR radars made multi-Doppler analysis possible (Fig. 20) at 1823 UTC. The multi-Doppler analysis at 1823 UTC depicted high-resolution CTD fields associated with the ongoing nonsupercell convective complex that were larger in magnitude than the observed fields, and the finer details of the CTD were not resolved by the mAMV analysis. It should be noted that all resolved overshooting tops in this radar analysis were captured as positive divergence regions, though the spatial location of the $5 \times 10^{-4}\,s^{-1}$ radar-derived divergence contour in Fig. 20 was located to the south and east of the SRSOR CTD even with a satellite parallax displacement correction. Despite the fact that there are position and magnitude errors possible with multi-Doppler experimentation at high altitudes in the atmosphere, further analyses with radar data will likely be beneficial for identifying small-scale flow fields in future studies to

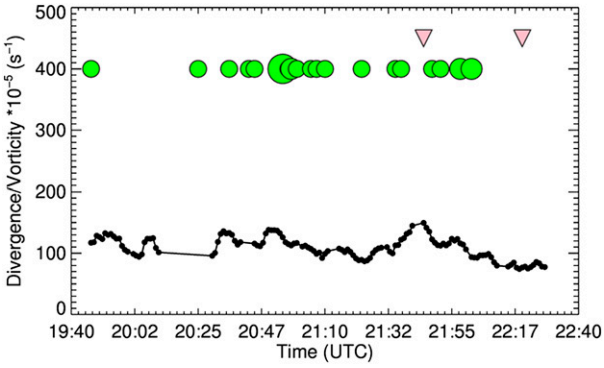

FIG. 16. The 22 May 2014 central Virginia supercell SRSOR CTD (black) and positive CTV (red) maximum values closest to the overshooting top identified by visible satellite data with SPC tornado reports (pink triangles) and hail reports scaled by size (green circles).

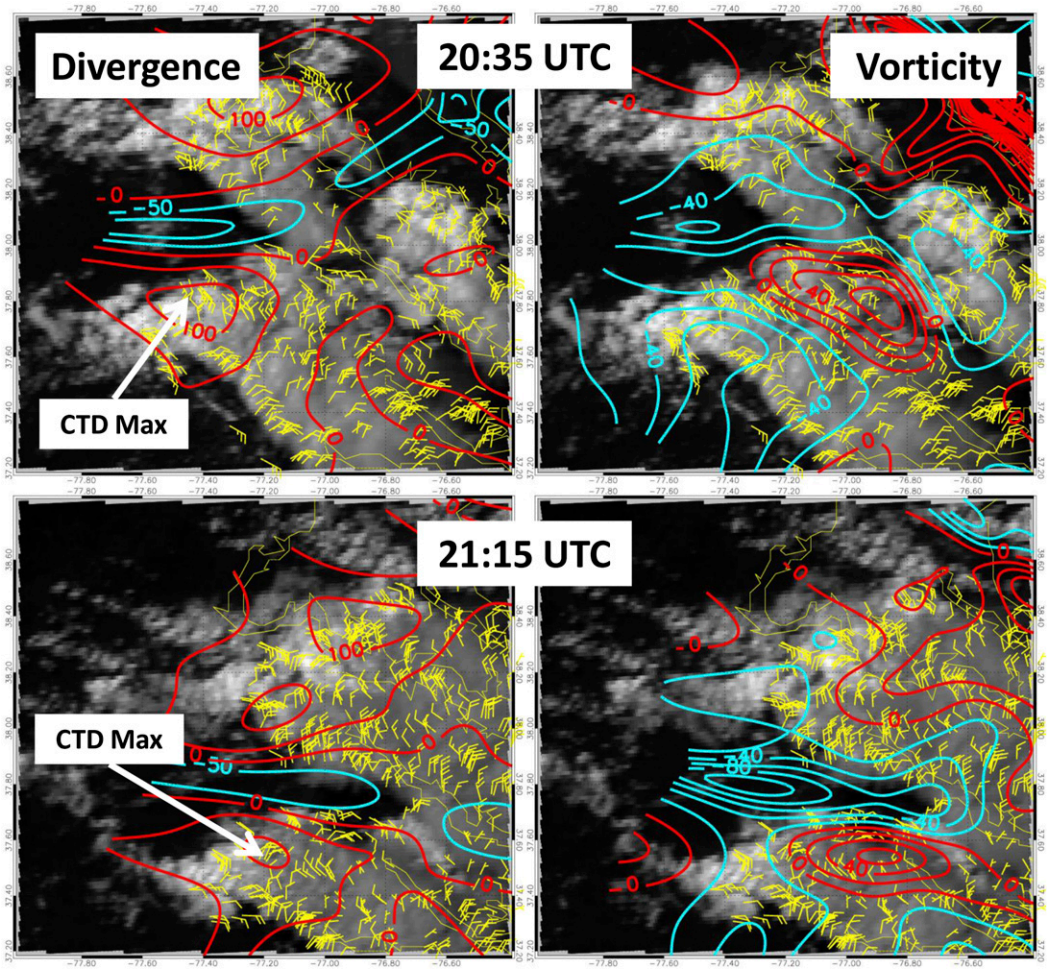

FIG. 17. As in Fig. 15, but over eastern Virginia.

optimize mAMV collection techniques and objective analysis methods for SRSOR CTD and CTV measurements.

g. *ARW simulation results*

As the primary formation mechanism and behavior of the CTV couplet signature observed are currently unknown, an ARW model simulation was run with the focus of identifying vorticity formations near the cloud top in varying storm modes, with the configurations used in this model experiment described above. The ARW simulation is also used to test the validity of the mAMV-observed flow signatures over the six cases of deep convection. Nonsupercell convection and supercell convection were produced in simulated nonvertically sheared and vertically sheared environments, respectively. Cloud tops are identified as the region at which vertical motion reaches zero ($w = 0$), which matches well with the parameterized total water content. Cross sections of vertical vorticity 42 min after the model initialization of the supercell show two distinct and deep cyclonic and anticyclonic columns (Fig. 21). A notable minimum in vorticity magnitude throughout these columns occurs near 13 km.

The 14-km planar-view images show that these idealized columns behave in a manner similar to those observed by SRSOR mAMVs, forming the so-called CTV couplet signature (Fig. 22). The ARW-resolved CTD follows the location of the maximum updraft speed. The level of streamwise vorticity present in hodograph A (Fig. 5a) allows for the ARW-resolved positive CTV location to be advected toward the divergence maximum, a pattern of behavior that is described by the advection component of the linearized vertical vorticity equation [Eq. (1)]. The CTD location over the positive CTV tendency was observed in the three CTV couplet signature cases analyzed with SRSOR mAMVs, which were all supercells propagating to the right of the environmental storm motion vector.

In addition to analyzing the vorticity fields from the ARW simulation, observations of mesoscale vorticity

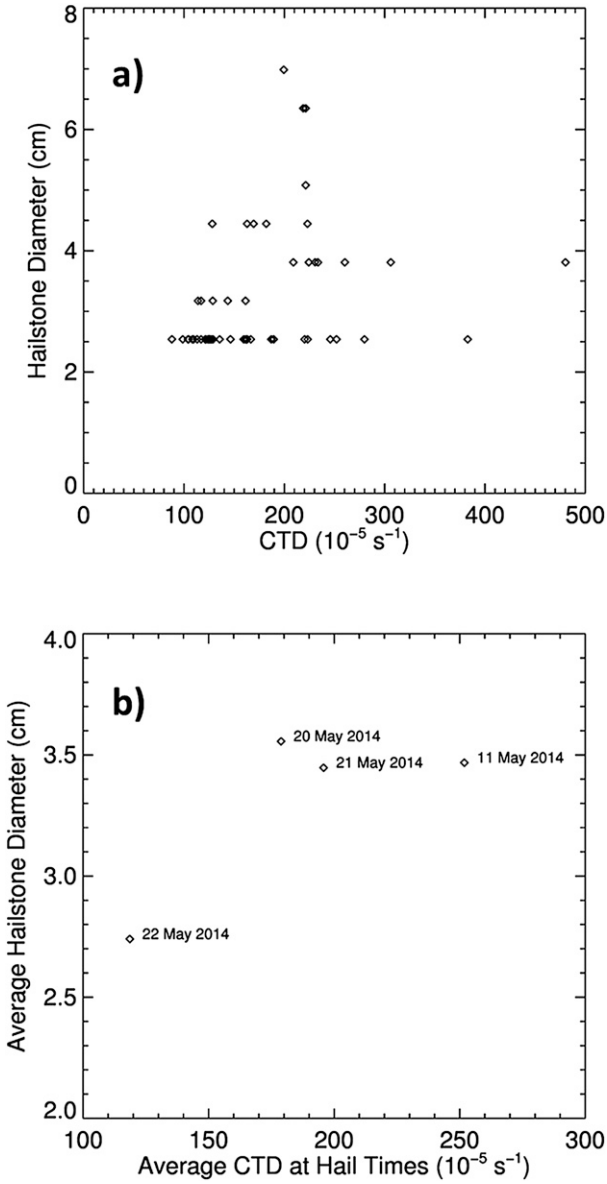

FIG. 18. (a) Hail diameter (cm) for all four supercell storms compared with average CTD value during a 10-min period prior to the SPC storm report and (b) total average hail size compared with total average CTD during a 10-min period prior to each report for each case study.

tendency show that the primary mechanism of vertical vorticity generation near the cloud top (14 km) is vorticity tilting (Fig. 23), which is consistent with previous findings of the principal mechanism of midtropospheric vertical vorticity generation in supercells (Rotunno and Klemp 1982). The observed vertical vorticity advection was small compared to the magnitudes of vorticity generation produced by tilting. Horizontal advection, coupled with vertical vorticity generation by tilting, acted to elongate the CTV couplet signature, which was a pattern of behavior notably similar to what is observed with SRSOR mAMV-derived flow. The elongation of the ARW-resolved vorticity downstream by horizontal advection shows a pattern of behavior that may aid in the detection of CTV couplet signatures with SRSOR mAMVs. The low response value of the currently used Barnes objective analysis (see appendix A) may not be a problem for strong, long-lived supercells as the CTV couplet signature elongates itself downstream to detectable spatial limits. Given the negative tendency associated with the stretching and horizontal advection components near the diverging cloud top, it is likely that these terms were the cause of the localized vorticity magnitude minima at 13 km in Fig. 21c. Stretching is also likely the tendency that causes larger vertical vorticity values to be observed downstream of the CTD maximum, rather than a direct juxtaposition, as horizontal divergence (convergence) reduces (increases) the current magnitude of the vertical vorticity values. The lack of solenoidal generation of vorticity highlights the lack of obstacle-flow-related influences [such as those suspected to be involved in the development of the enhanced-V signature in GOES IR imagery; Brunner et al. (2007)] on the development of the vertical vorticity in the CTV couplet signature and is consistent with previous works on the dynamics of supercells (Rotunno and Klemp 1982; Wiesmann and Klemp 1982, 1984).

The same planar and cross-sectional views are analyzed with a nonsupercell storm with no mean flow (Figs. 24 and 25). Without shear, while positive divergence forms at the location of the updraft, no large value of vorticity forms near the cloud top. Furthermore, the updraft is short lived, as divergence at 14 km decreases by minute 50 in the simulation. The cross sections through the updraft show little in the way of cyclonic or anticyclonic vertical vorticity values through the depth of the storm, with divergence that peaks at the cloud top where w approaches zero.

A final note on the magnitude of the CTD and CTV signatures for ARW-modeled versus observed mAMVs over supercell storms suggests that there is some degree of wind field smoothing occurring with the Barnes objectively analyzed satellite data. Maximum values of CTD derived within the ARW framework exceeded 0.02 s^{-1}, which is consistent with the observed values suggested by Witt and Nelson (1991). In the observational study presented here, on average the supercells exhibited SRSOR mAMV-derived CTD values closer to 0.002, approximately one order of magnitude less than simulated maxima. The selected ARW grid has the ability to model features of ~1 km in size with 200-m grid-point spacing, while as shown in appendix A,

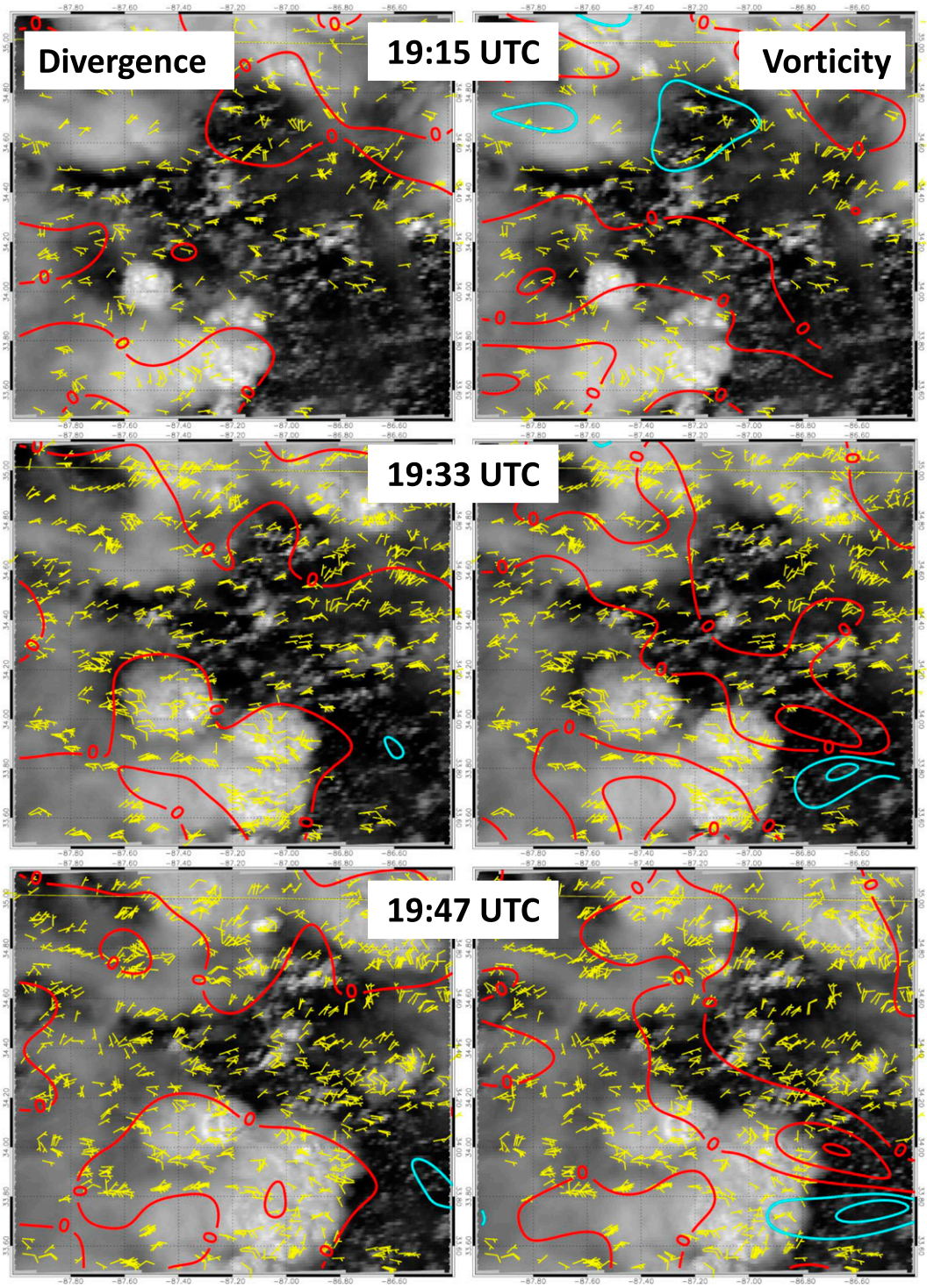

FIG. 19. As in Fig. 7, but for 18 Aug 2014 over northern Alabama.

the Barnes objective analysis cannot resolve features below ~20 km. The current Barnes falloff and convergence parameters are set based on the average spatial density of the derived mAMVs, which determine the lower length-scale limit of the resolvable features. Experimentation of SRSOR mAMV values with higher spatial resolution satellite products, where more mAMVs can be acquired (and hence lower falloff parameters can

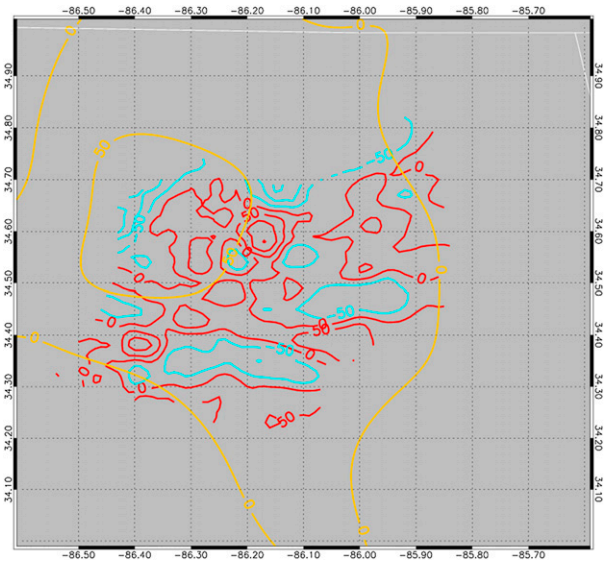

FIG. 20. The 1823 UTC 18 Aug 2014 SRSOR CTD contoured with positive values as yellow and 9-km divergence from multi-Doppler analysis using KHTX and ARMOR contoured with the same intervals as in Fig. 7.

be used), will likely yield higher observable values of SRSOR CTD and CTV that match the depiction of the flow put forward by the ARW simulations and multi-Doppler analysis fields.

5. Discussion and conclusions

For the present study, the original mAMV algorithm of Bedka and Mecikalski (2005) was repurposed to observe deep convective cloud-top motions at high temporal resolution by satellite. The results produced high temporal resolution flow analyses of the cloud tops of deep convection. Using divergence and vertical vorticity fields from mAMVs objectively analyzed to a grid, a convection analyst can infer properties of a storm. Through comparison of six case studies, four supercells, one QLCS, and one nonsupercell convective event, CTD properties were found to differ considerably. Nonsupercell convection observed in this sample of storms produced weak, nonpersistent CTD signals, which quickly disperse as the systems dissipated. The QLCS exhibited similar characteristics in divergence to nonsupercell convection; however, when the systems grew upscale into MCSs, a clear linear divergence signal could be seen. The linear divergence signal had nonpersistent CTD maxima that typically lasted 10–30 min along the convective line. Maxima in the CTD were roughly collocated to overshooting tops and divergence patterns diagnosed through multi-Doppler wind flow analysis. The geometry and magnitude of the flow fields derived in the multi-Doppler analysis suggest that the

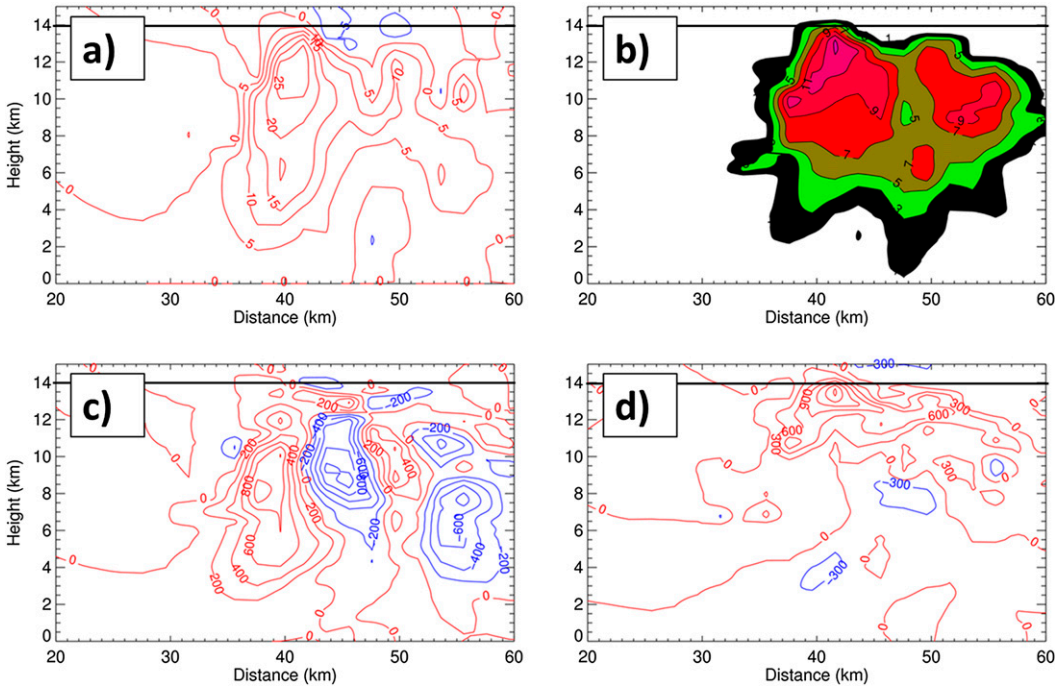

FIG. 21. The 42-min ARW hodograph A output (quarter-circle shear; see Fig. 5) south-to-north cross section at $x = 52$ km (shown in Fig. 22, below) with (a) w (m s^{-1}), (b) total water content (cloud water, cloud ice, snow, graupel, and rainwater; g m^{-3}), (c) vertical vorticity contoured every 200×10^{-5} s^{-1}, and (d) divergence contoured every 300×10^{-5} s^{-1}. The line indicates the height of the plan view in Fig. 22, below. Values were calculated using 2 km × 2 km averaged grids to smooth the effects of turbulence.

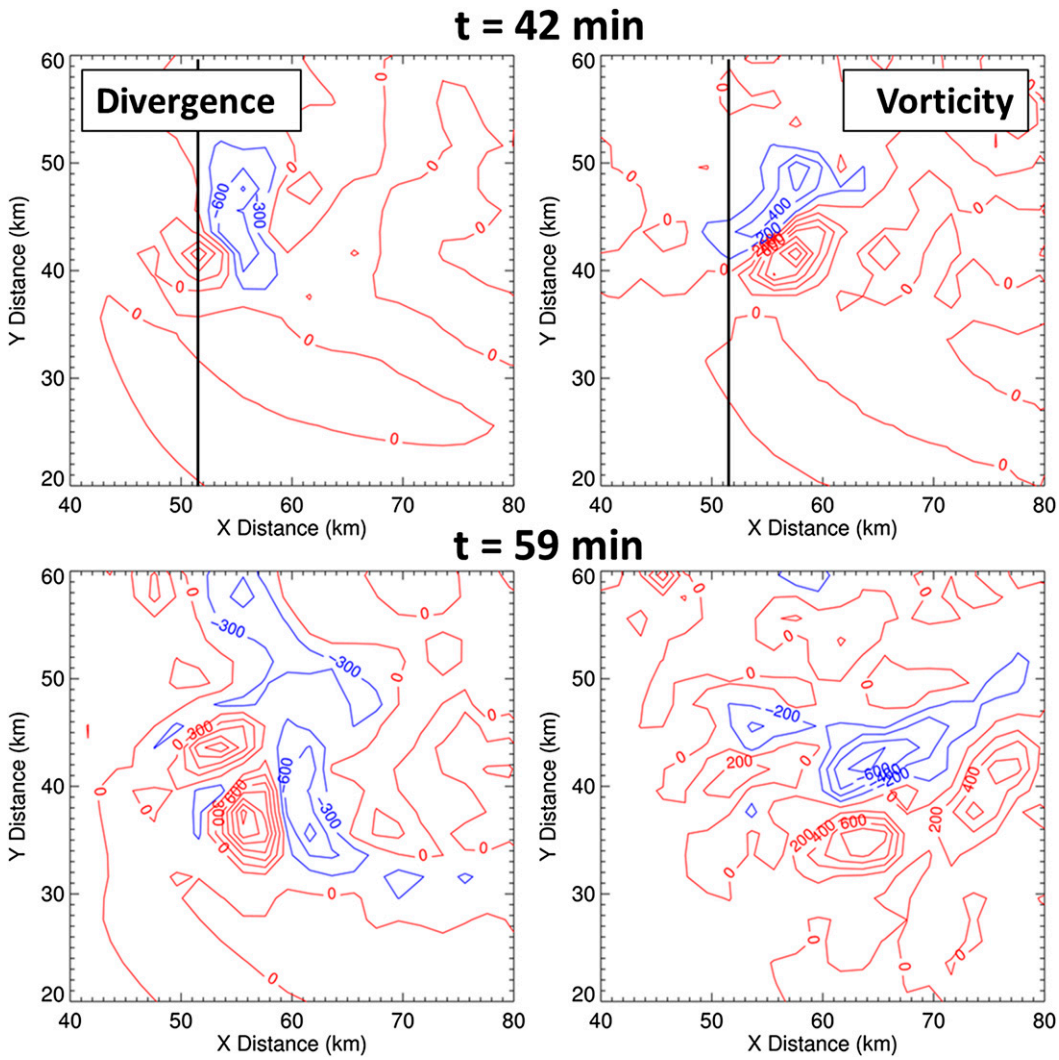

FIG. 22. The 42- and 59-min ARW hodograph A output (quarter-circle shear; see Fig. 5) plan view at a height z = 14 km with (left) divergence contoured every $300 \times 10^{-5}\,\mathrm{s}^{-1}$ for cleanliness and (right) vertical vorticity contoured every $200 \times 10^{-5}\,\mathrm{s}^{-1}$. The black line indicates the location of the cross section in Fig. 21. Values were calculated using 2 km × 2 km averaged grids to smooth the effects of turbulence.

current Barnes objective analysis may be smoothing over some of the finer storm-scale features of CTD maxima. However, given the errors inherent with the assumptions made to derive horizontal flow from ground-based Doppler radar data at high altitudes, an improved upper-level radar sampling method, or perhaps a model-based observing systems simulation experiment, will be required to optimize objective analysis methods for SRSOR mAMV convective cloud-top flow field derivation.

Given the similarities in the products measured, it is hypothesized that CTD, when produced with mAMVs that were "uncontaminated" by the surrounding mesoscale flow, is a similar indirect measurement of updraft strength, as indicated by single-Doppler radar-based analysis (Witt and Nelson 1991). Theoretically, CTD should be related to updraft strength through mass continuity. Use of a larger storm sample size would be needed to determine a statistical relationship between CTD and hail size and how that can best be incorporated into severe weather nowcasting algorithms. Although no obvious correspondence was found between the satellite flow metrics derived here and the formation of tornadoes at the ground, it is possible that combining SRSOR mAMV-derived CTD and CTV results with other satellite metrics such as overshooting tops, enhanced-V signatures, and ground-based measurements such as those made from radar and wind profilers may yield

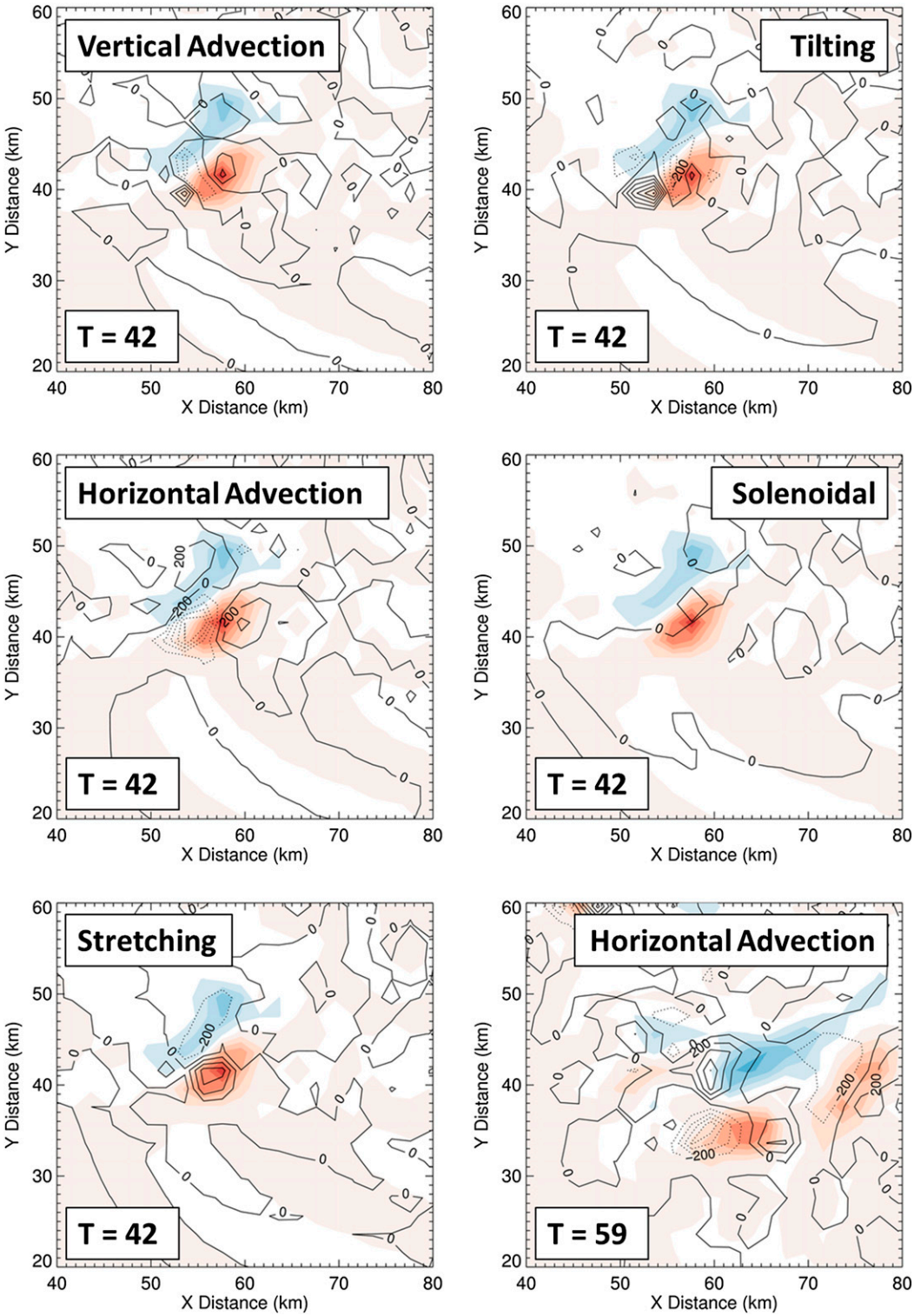

FIG. 23. The 42-min ARW hodograph A (quarter-circle shear; see Fig. 5) plan view of vorticity equation variables at $z = 14$ km, contoured every $200 \times 10^{-7}\,\mathrm{s}^{-2}$ with color-shaded vertical vorticity, with red representing cyclonic and blue representing anticyclonic flow patterns. (bottom right) The horizontal advection term at 59 min. Values were calculated using 2 km × 2 km averaged grids to smooth the effects of turbulence.

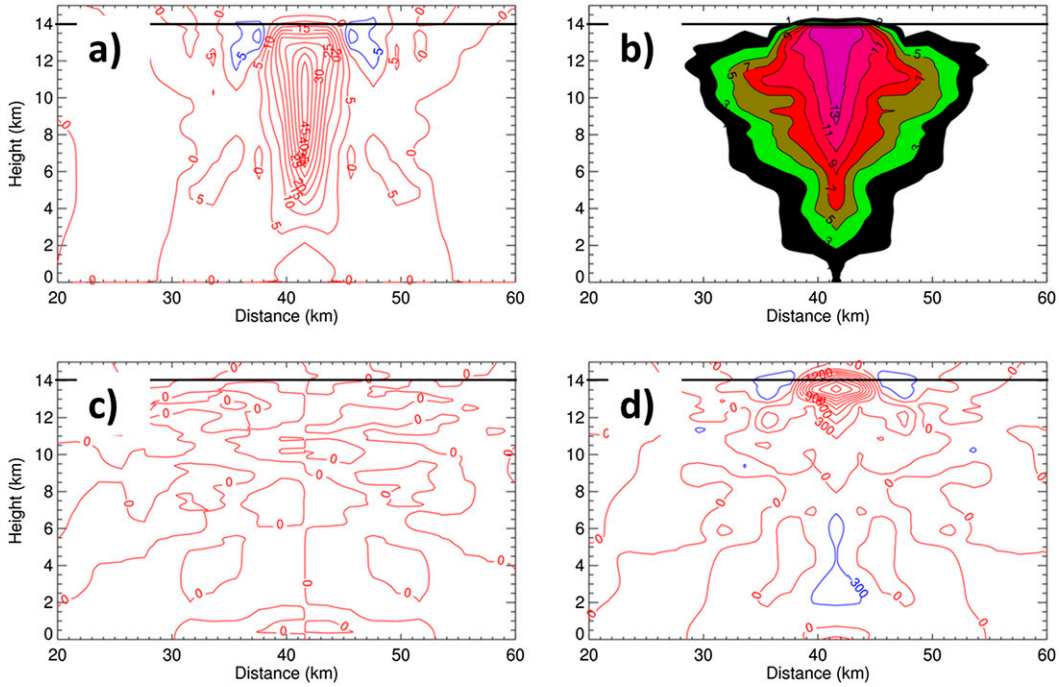

FIG. 24. The 33-min ARW hodograph B output (no vertical wind shear; see Fig. 5) south-to-north cross section at $x = 42$ km with (a) w (m s^{-1}), (b) total water content (cloud water, cloud ice, snow, graupel, and rainwater; g m^{-3}), (c) vertical vorticity contoured every 200×10^{-5} s^{-1}, and (d) divergence contoured every 300×10^{-5} s^{-1}. The black line indicates the location of the plan view in Fig. 25, below. Values were calculated using 2 km × 2 km averaged grids to smooth the effects of turbulence.

new knowledge of the tornadogenesis process as it relates to the overall storm structure.

It is found that three out of the four supercell cases produced observable CTV couplet patterns. Analysis with ARW-idealized simulations of supercell and non-supercell convection suggests that CTV couplet signatures witnessed by GOES are associated with supercells only. Using the results from idealized ARW-modeled supercell

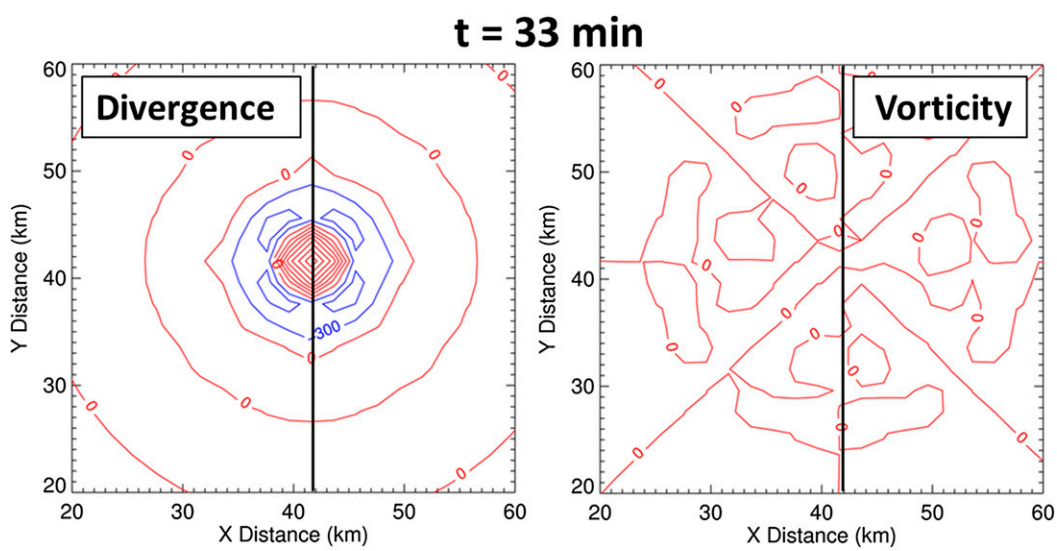

FIG. 25. The 33-min ARW hodograph A output (no shear; see Fig. 5) plan view at a height $z = 14$ km with (left) divergence contoured every 300×10^{-5} s^{-1} and (right) vertical vorticity contoured every 200×10^{-5} s^{-1}. The black lines indicate the locations of the cross sections in Figs. 24a–d. Values were calculated using 2 km × 2 km averaged grids to smooth the effects of turbulence.

convection, it was shown that the primary mechanism behind the development of the CTV couplet signature, when analyzing the individual components of vertical vorticity generation near cloud top, was tilting near the location of the updraft. A lack of solenoidal vorticity generation or vertical vorticity advection leads us to conclude that obstacle flow mechanisms are not the primary contributor to observed mAMV atmospheric vertical vorticity at the cloud top. Thus the main conclusion of this work is that *persistent (lasting > 30 min) and large CTD maxima with CTV couplet signatures are observations unique to supercell storms and can be derived by only using satellite-based mAMV information.* Large values of CTD are dependent on the objective analysis used to derive the flow field. With the Barnes analysis used here, the sampled supercells commonly exhibited CTD values $> 7.5 \times 10^{-4}$. It is important to note the impact of using a more coarse temporal resolution on the derivation of mAMV data and subsequently on the derived cloud-top flow fields. As shown in Fig. 1, a coarse set of image triplets produces very few mAMVs in the deep convective cloud top for a cross-correlation-based mAMV scheme, which, as discussed in appendix A, would result in the need to use large smoothing parameters in the Barnes analysis that may subsequently prevent the resolution of cloud-top signals seen in this study. The persistent CTD maxima and CTV couplet signatures shown in this study were only resolved with a very fine (1 min) temporal resolution.

Several issues related to a flow-based mAMV analysis need to be addressed prior to operational use by forecasters. Scenarios involving multideck mAMV detection created problematic flow fields on the cloud edges, where vertical wind shear created substantial signatures of both divergence and vorticity. These signatures, when not witnessed directly on the cloud top, were simple to subjectively identify; however, they are difficult to objectively remove from the mAMV algorithm output without more advanced height assignment procedures involving cloud masks. One of the first steps taken in this study was to remove any mAMVs witnessed below 500 hPa using T_B thresholds and GFS sounding data. If higher-altitude thresholds were used (such as that shown in appendix B), vectors along or near the edges of mature deep convection would be lost, given the optically thin nature of the cloud yielding the warmer temperatures of the ground. Newer versions of the mAMV-derived flow algorithm will include more advanced low target identification schemes to remove false CTV and CTD values. Further issues stemmed from cirrus contamination of a particular sample, such as the 22 May 2014 storm over Delaware sampled here.

Future studies will provide the means to validate different systems of mAMV-generating programs. While vector analysis optimization was beyond the scope of this study, further work will also examine mesoscale versions for the proposed GOES-R operational AMV algorithm in Bresky et al. (2012), pending the success of the mesoscale AMV version of this proof of concept. Introducing a new methodology may reduce the loss of vectors from a lack of target information. Use of an alternative objective analysis with varied scaling such as the RF analysis (Hayden and Purser 1995) may also resolve issues associated with nonuniform point source mAMV grids seen with the large data gaps from the 11 and 21 May 2014 case studies. Such objective analyses will be tested with multi-Doppler collections for optimal derivation methods of SRSOR mAMV-based CTD and CTV results. Work is also under way to collect additional SRSOR supercell case studies in regions with dense data coverage, including lightning mapping arrays and multi-Doppler networks like those in northern Alabama and northern Colorado, with a focus on identifying why some supercells do not produce the CTV couplet signatures, such as the 22 May 2014 case, and what storm characteristics may cause enhancements in CTD and storm electrification.

Acknowledgments. This work was funded by National Science Foundation Grant AGS-1261368. We thank Dr. Dan Lindsey at the Cooperative Institute for Research in the Atmosphere for providing several of the required super rapid scan satellite datasets used in this work. In addition, we thank Chris Velden, Kris Bedka, Dr. Udaysankar Nair, Andrew White, Timothy Schmit, Dr. Steve Goodman, and Dr. Paul Markowski for their input and thoughtful evaluation of our observations and conclusions. We also extend our gratitude to the three anonymous reviewers and our editor Dr. Paquita Zuidema, whose time and thoughtful comments substantially improved the quality of this paper. The ARW modeling aspect was completed in part as a class project for ATS-651 Atmospheric Fluid Dynamics II at the University of Alabama in Huntsville. Current SRSOR datasets can be found online (http://cimss.ssec.wisc.edu/goes/srsor2016/GOES-14_SRSOR.html).

APPENDIX A

Objective Analysis Parameter Estimation

The selection of the "falloff" parameter in this paper followed the method outlined by Koch et al. (1983). The response function of the Barnes (1973) analysis is given by

$$D = D_o(1 + D_o^{\gamma-1} - D_o^{\gamma}), \quad \text{(A1)}$$

where D_o is given by the first-pass response function,

$$D_o = \exp[-c(\pi/\lambda)^2], \quad \text{(A2)}$$

and γ, λ, and c are the convergence parameter, wavelength, and falloff parameter, respectively, and π retains its normal definition as the constant ratio of the circumference of a circle to its diameter. The 11 May 2014 case was the first to be examined while the storms were in a mature phase at 2122 UTC with several mAMVs within our examined domain. Using Eq. (12) from Koch et al. (1983) for M number of vectors in an area of size A, uniform spacing (S) would be

$$S = A^{0.5}[(1 + M^{0.5})/(M - 1)]. \quad \text{(A3)}$$

At 2122 UTC, there were 618 vectors measured in one set of 1-min triplets (this does not include all mAMVs over the 5-min time-smoothing period) within the 20 000 km^2 area. This yielded a uniform average S value of ~18.74 km. Using S with Eq. (13) in Koch et al. (1983) gave the falloff parameter as

$$c = 5.052(2S/\pi)^2. \quad \text{(A4)}$$

For the measurement time period, the falloff parameter c value was 7.19×10^8. The 2123 UTC time frame produced a c value of 8.92×10^8. This analysis was performed for several 1-min mAMV image triplets, producing an average of about 8×10^8.

The value of γ was chosen subjectively to retain as much detail as possible with an acceptable level of noise. Koch et al. (1983) suggested using values between 0.2 and 1, with 0.2 providing the maximum amount of detail. Through observation of the 20 May 2014 case compared to subjective observations such as those in Fig. 1a, we showed that $\gamma = 0.3$ maintained an acceptable amount of detail in the flow field with a minimum amount of noise. Analyzing the plot of the response function Eq. (A1) with respect to wavelength with the chosen values of γ and c suggests that the wavelengths resolved in the supercell cases (which varied from ~40 to 60 km) were only ~20%–60% of the actual amplitude of the observed disturbances (Fig. A1). Hence, the current Barnes analysis should be underestimating the CTD and CTV magnitudes of the thunderstorms observed here, which is seen when comparing SRSOR-derived mAMV flow fields to multi-Doppler and model observations of CTD and CTV.

The average overall mAMV data spacing is determined to be around 2 km, which with a 0.01° resolution (~1 km) produces grid-spacing ratios (the ratio of the grid spacing and the data spacing) near 0.5. In data-rich regions with time smoothing, the average mAMV grid spacing drops to ~0.5–1 km, which is typical in the deep convective cases analyzed here. Koch et al. (1983) explains that grid spacing ratios larger than 0.5 suggest that there are fewer than five data points to resolve the minimum possible wave, which emphasizes the need to have more mAMVs available by way of time smoothing. Once more targets are identified with new mAMV collection techniques using the enhanced ~500-m visible and ~2-km IR resolution Advanced Baseline Imager instrument on the GOES-R satellite, the γ and c parameters can be adjusted to yield a higher percentage of shorter wave amplitudes (lower values of c) without the consequence of producing erratic fields that are sensitive to mAMV availability.

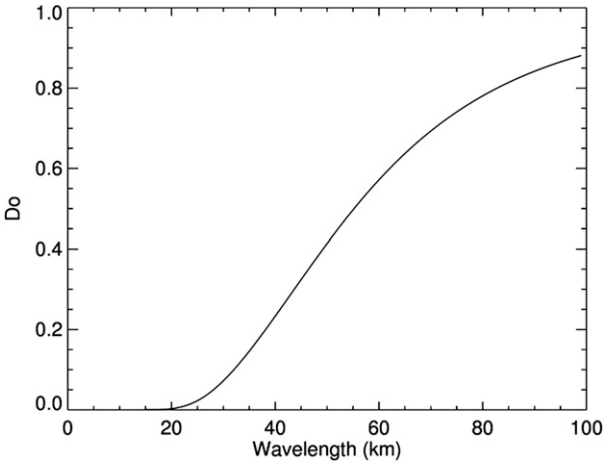

FIG. A1. Barnes response function for varying wavelengths (km) using γ and c values of 0.3 and 8×10^8, respectively.

APPENDIX B

The Effects of Cirrus Contamination and Barnes Analysis Oversmoothing

Flow fields measured in this paper may have been impacted by the contamination of motions from nearby unrelated clouds, either as a result of cirrus or remaining low-level motions in the mAMV analysis. To examine the impact of oversmoothing by the Barnes analysis from incorrectly measured cloud-top anvil motions, the 11 May 2013 case at 2123 UTC was analyzed in further detail, where the pressure cutoff is now moved from 500 to 350 hPa (Fig. B1). By implementing a lower pressure cutoff for the mAMV cloud-top analysis, some of the low-cloud contamination was removed from the Barnes analysis, which has the effect of shifting the location of the CTD maximum. Note that in area A in Fig. B1, and also in Fig. 7, the magnitude of the divergence and vorticity remains largely unchanged despite the removal

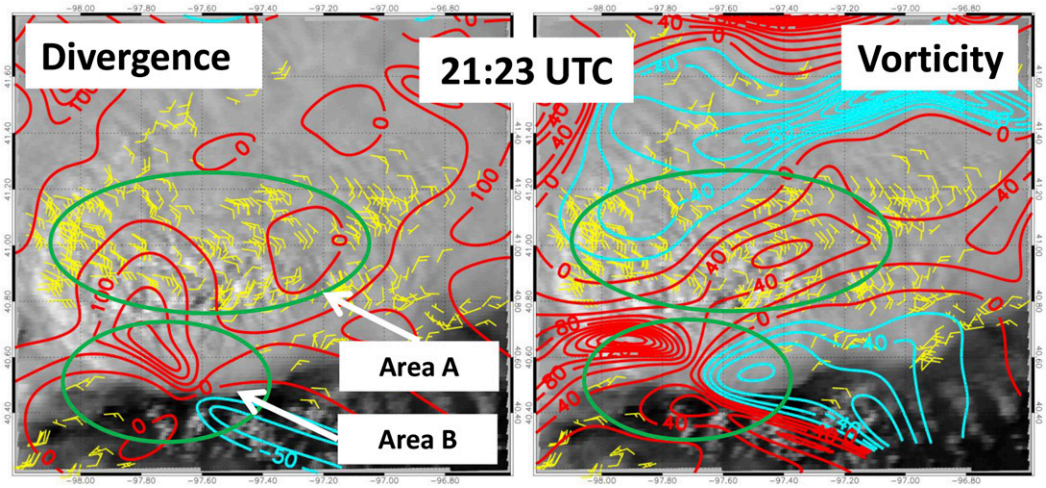

FIG. B1. Selected 11 May 2014 SRSOR GOES visible satellite data plotted following the same convention as in Fig. 7, with a Barnes objective analysis performed for vectors above 350 hPa. Areas in the green circles are referenced in the text, with vectors that are kept (area A) and removed (area B) changing the objective analysis.

of lower-level mAMVs nearby. However, in area B, which contains the CTD maximum at this time, the location and magnitude of the CTD changes as a result of the removal of the vectors. Thus, the conclusion from this analysis is that the values for the maximum CTD shown in the time series may at times be affected by low-level contamination, causing unusually high (or perhaps at times low) maxima values. While the values of CTD may be related to updraft strength with time, this 11 May 2014 example highlights the importance of implementing cloud masks for future products to ensure that all vectors used for an objective analysis are in fact associated with deep convective cloud tops only (i.e., cirrus vs lower-level cumulus or other cloud types). The problem with implementing a higher-altitude mAMV cutoff as performed in Fig. B1 for all cases is that several supercells, including those of 20 May 2014 and 21 May 2014, had thin cirrus cloud edges at anvil level that were incorrectly assigned to lower altitudes in the mAMV derivation process, and thus are lost when using a cutoff below 500 hPa. Hence, the 500-hPa cutoff was used to maintain the anvil-level mAMV spatial density, the importance of which is described in appendix A, in the supercell cases seen here.

A second example demonstrates the problem of cirrus contamination on the measurement of mAMVs in deep convective anvils for the storm system over Delaware on 22 May 2014 (Fig. B2). While most cases examined in

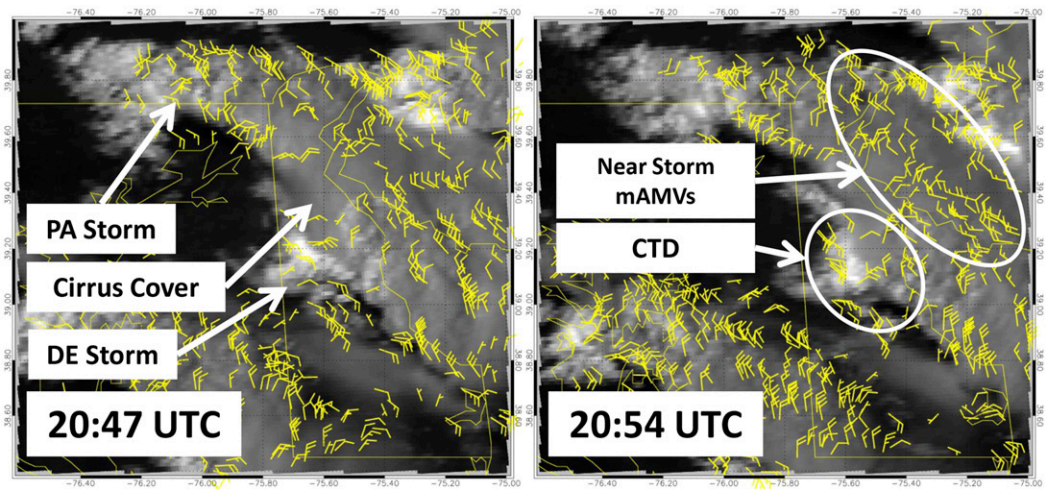

FIG. B2. The 22 May 2014 SRSOR *GOES-14* visible satellite data at two times with equilibrium-level-relative mAMVs highlighting cirrus contamination of the storm in Delaware from a similar storm to the north in Pennsylvania.

this dataset were discrete supercells in nature, it is apparent that cirrus from other adjacent storm systems or within the larger synoptic-scale environment can overrun or cover parts of a deep convective anvil, acting to mask targets important to the observation of the overall storm-top flows. Problems caused by cirrus contamination can perhaps be solved with optical-depth-based AMV algorithms for deriving motions beneath thin cirrus clouds.

Oversmoothing of nearby cirrus vectors may have also been a problem with our dataset, in a similar manner to the low-level mAMV contamination on 11 May 2014. One possible solution with future mAMV products involves using smaller falloff parameters that smooth over finer scales as the density of targets improves with the use of GOES-R data and new mAMV collection techniques. Different objective analysis techniques may also mitigate problems of nearby vector contamination and problems caused by nonuniform grids such as RFs that allow for varied scaling across grid space (Hayden and Purser 1995). Another solution to near-storm mAMV contamination involves objective segmentation of identified cloud objects such as those in Lakshmanan and Smith (2009) and Sieglaff et al. (2013) to cluster individual storm flow fields together and truncate near-storm vectors from objective analysis derivation. Objective analysis optimization for deep convective cloud-top flow estimation will likely take place after the launch of GOES-R when a sample of 30-s time-step rapid scan mAMVs can be collected within a reliable ground-based multi-Doppler radar dataset similar to that collected for the 18 August 2014 case study.

REFERENCES

Barnes, S. L., 1964: A technique for maximizing details in numerical weather map analysis. *J. Appl. Meteor.*, **3**, 396–409, doi:10.1175/1520-0450(1964)003<0396:ATFMDI>2.0.CO;2.

——, 1973: Mesoscale objective map analysis using weighted time-series observations. NOAA Tech. Memo. ERL NSSL-62, 60 pp. [Available online at http://docs.lib.noaa.gov/noaa_documents/OAR/NSSL/NOAA_TM_ERL_NSSL/ERL_NSSL_62.pdf.]

Bedka, K. M., and J. R. Mecikalski, 2005: Application of satellite-derived atmospheric motion vectors for estimating mesoscale flows. *J. Appl. Meteor.*, **44**, 1761–1772, doi:10.1175/JAM2264.1.

——, C. S. Velden, R. A. Petersen, W. F. Feltz, and J. R. Mecikalski, 2009: Comparisons of satellite-derived atmospheric motion vectors, rawinsondes, and NOAA wind profiler observations. *J. Appl. Meteor. Climatol.*, **48**, 1542–1561, doi:10.1175/2009JAMC1867.1.

——, C. Wang, R. Rogers, L. D. Carey, W. Feltz, and J. Kanak, 2015: Examining deep convective cloud evolution using total lightning, WSR-88D, and *GOES-14* super rapid scan datasets. *Wea. Forecasting*, **30**, 571–590, doi:10.1175/WAF-D-14-00062.1.

Biggerstaff, M. I., and Coauthors, 2005: The Shared Mobile Atmospheric Research and Teaching radar: A collaboration to enhance research and teaching. *Bull. Amer. Meteor. Soc.*, **86**, 1263–1274, doi:10.1175/BAMS-86-9-1263.

Bluestein, H. B., A. L. Pazmany, J. C. Galloway, and R. E. Mcintosh, 1995: Studies of the substructure of severe convective storms using a mobile 3-mm-wavelength Doppler radar. *Bull. Amer. Meteor. Soc.*, **76**, 2155–2169, doi:10.1175/1520-0477(1995)076<2155:SOTSOS>2.0.CO;2.

——, M. M. French, I. PopStefanija, R. T. Bluth, and J. B. Knorr, 2010: A mobile, phased-array Doppler radar for the study of severe convective storms. *Bull. Amer. Meteor. Soc.*, **91**, 579–600, doi:10.1175/2009BAMS2914.1.

Brandes, E. A., 1977: Gust front evolution and tornado genesis as viewed by Doppler radar. *J. Appl. Meteor.*, **16**, 333–338, doi:10.1175/1520-0450(1977)016<0333:GFEATG>2.0.CO;2.

——, 1978: Mesocyclone evolution and tornadogenesis: Some observations. *Mon. Wea. Rev.*, **106**, 995–1011, doi:10.1175/1520-0493(1978)106<0995:MEATSO>2.0.CO;2.

——, 1981: Fine structure of the Del City-Edmond tornadic mesocirculation. *Mon. Wea. Rev.*, **109**, 635–647, doi:10.1175/1520-0493(1981)109<0635:FOTDCE>2.0.CO;2.

——, 1984a: Relationships between radar-derived thermodynamic variables and tornadogenesis. *Mon. Wea. Rev.*, **112**, 1033–1052, doi:10.1175/1520-0493(1984)112<1033:RBRDTV>2.0.CO;2.

——, 1984b: Vertical vorticity generation and mesocyclone sustenance in tornadic thunderstorms: The observational evidence. *Mon. Wea. Rev.*, **112**, 2253–2269, doi:10.1175/1520-0493(1984)112<2253:VVGAMS>2.0.CO;2.

——, R. P. Davies-Jones, and B. C. Johnson, 1988: Streamwise vorticity effects on supercell morphology and persistence. *J. Atmos. Sci.*, **45**, 947–963, doi:10.1175/1520-0469(1988)045<0947:SVEOSM>2.0.CO;2.

Bresky, W. C., J. M. Daniels, A. A. Bailey, and S. T. Wanzong, 2012: New methods toward minimizing the slow speed bias associated with atmospheric motion vectors. *J. Appl. Meteor. Climatol.*, **51**, 2137–2151, doi:10.1175/JAMC-D-11-0234.1.

Browning, K. A., 1964: Airflow and precipitation trajectories within severe local storms which travel to the right of the winds. *J. Atmos. Sci.*, **21**, 634–639, doi:10.1175/1520-0469(1964)021<0634:AAPTWS>2.0.CO;2.

——, 1965: Some inferences about the updraft within a severe local storm. *J. Atmos. Sci.*, **22**, 669–677, doi:10.1175/1520-0469(1965)022<0669:SIATUW>2.0.CO;2.

Brunner, J. C., S. A. Ackerman, A. S. Bachmeier, and R. M. Rabin, 2007: A quantitative analysis of the enhanced-V feature in relation to severe weather. *Wea. Forecasting*, **22**, 853–872, doi:10.1175/WAF1022.1.

Bryan, G. H., J. C. Wyngaard, and J. Michael Fritsch, 2003: Resolution requirements for the simulation of deep moist convection. *Mon. Wea. Rev.*, **131**, 2394–2416, doi:10.1175/1520-0493(2003)131<2394:RRFTSO>2.0.CO;2.

Cintineo, J. L., M. J. Pavolonis, J. M. Sieglaff, and D. T. Lindsey, 2014: An empirical model for assessing the severe weather potential of developing convection. *Wea. Forecasting*, **29**, 639–653, doi:10.1175/WAF-D-13-00113.1.

Cintineo, R. M., and D. J. Stensrud, 2013: On the predictability of supercell thunderstorm evolution. *J. Atmos. Sci.*, **70**, 1993–2011, doi:10.1175/JAS-D-12-0166.1.

Cressman, G. P., 1959: An operational objective analysis system. *Mon. Wea. Rev.*, **87**, 367–374, doi:10.1175/1520-0493(1959)087<0367:AOOAS>2.0.CO;2.

Dance, S., E. Ebert, and D. Scurrah, 2010: Thunderstorm strike probability nowcasting. *J. Atmos. Oceanic Technol.*, **27**, 79–93, doi:10.1175/2009JTECHA1279.1.

Davies-Jones, R., J. Trapp, and H. B. Bluestein, 2001: Tornadoes and tornadic storms. *Severe Convective Storms*, *Meteor. Monogr.*, No. 50, Amer. Meteor. Soc., 167–222.

French, M. M., H. B. Bluestein, I. PopStefanija, C. A. Baldi, and R. T. Bluth, 2014: Mobile, phased-array, Doppler radar observations of tornadoes at X band. *Mon. Wea. Rev.*, **142**, 1010–1036, doi:10.1175/MWR-D-13-00101.1.

Fujita, T., 1968: Present status of cloud velocity computations from ATS-1 and ATS-3. *Ninth Plenary Meeting on Space Research*, Tokyo, Japan, COSPAR, 557–570.

Hayden, C. M., and R. J. Purser, 1995: Recursive filter objective analysis of meteorological fields: Applications to NESDIS operational processing. *J. Appl. Meteor.*, **34**, 3–15, doi:10.1175/1520-0450-34.1.3.

Holmlund, K., 1998: The utilization of statistical properties of satellite-derived atmospheric motion vectors to derive quality indicators. *Wea. Forecasting*, **13**, 1093–1104, doi:10.1175/1520-0434(1998)013<1093:TUOSPO>2.0.CO;2.

Hu, S., S. Gu, X. Zhuang, and H. Luo, 2007: Automatic identification of storm cells using Doppler radars. *Acta Meteor. Sin.*, **21**, 353–365.

Hubert, L. F., and L. F. Whitney Jr., 1971: Wind estimation from geostationary-satellite pictures. *Mon. Wea. Rev.*, **99**, 665–672, doi:10.1175/1520-0493(1971)099<0665:WEFGP>2.3.CO;2.

Klemp, J., 1987: The dynamics of severe thunderstorms. *Annu. Rev. Fluid Mech.*, **19**, 369–402, doi:10.1146/annurev.fl.19.010187.002101.

Koch, S. E., M. desJardins, and P. J. Kocin, 1983: An interactive Barnes objective map analysis scheme for use with satellite and conventional data. *J. Climate Appl. Meteor.*, **22**, 1487–1503, doi:10.1175/1520-0450(1983)022<1487:AIBOMA>2.0.CO;2.

Kumjian, M. R., and A. V. Ryzhkov, 2008: Polarimetric signatures in supercell thunderstorms. *J. Appl. Meteor. Climatol.*, **47**, 1940–1961, doi:10.1175/2007JAMC1874.1.

——, Z. J. Lebo, and H. C. Morrison, 2015: On the mechanisms of rain formation in an idealized supercell storm. *Mon. Wea. Rev.*, **143**, 2754–2773, doi:10.1175/MWR-D-14-00402.1.

Lakshmanan, V., and T. Smith, 2009: Data mining storm attributes from spatial grids. *J. Atmos. Oceanic Technol.*, **26**, 2353–2365, doi:10.1175/2009JTECHA1257.1.

——, ——, G. J. Stumpf, and K. Hondl, 2007: The Warning Decision Support System–Integrated Information. *Wea. Forecasting*, **22**, 596–612, doi:10.1175/WAF1009.1.

Lemon, L. R., and C. A. Doswell III, 1979: Severe thunderstorm evolution and mesocyclone structure as related to tornadogenesis. *Mon. Wea. Rev.*, **107**, 1184–1197, doi:10.1175/1520-0493(1979)107<1184:STEAMS>2.0.CO;2.

Marwitz, J. D., 1972: The structure and motion of severe hailstorms. Part I: Supercell storms. *J. Appl. Meteor.*, **11**, 166–179, doi:10.1175/1520-0450(1972)011<0166:TSAMOS>2.0.CO;2.

Mecikalski, J. R., and K. M. Bedka, 2006: Forecasting convective initiation by monitoring the evolution of moving cumulus in daytime GOES imagery. *Mon. Wea. Rev.*, **134**, 49–78, doi:10.1175/MWR3062.1.

——, ——, S. J. Paech, and L. A. Litten, 2008: A statistical evaluation of GOES cloud-top properties for nowcasting convective initiation. *Mon. Wea. Rev.*, **136**, 4899–4914, doi:10.1175/2008MWR2352.1.

——, J. K. Williams, C. P. Jewett, D. Ahijevych, A. Leroy, and J. Walker, 2015: Probabilistic 0–1-h convective initiation nowcasts that combine geostationary satellite observations with numerical weather prediction model data. *J. Appl. Meteor. Climatol.*, **54**, 1039–1059, doi:10.1175/JAMC-D-14-0129.1.

Mohr, C. G., L. J. Miller, R. L. Vaughan, and H. W. Frank, 1986: The merger of mesoscale datasets into a common Cartesian format for efficient and systematic analyses. *J. Atmos. Oceanic Technol.*, **3**, 143–161, doi:10.1175/1520-0426(1986)003<0143:TMOMDI>2.0.CO;2.

Morrison, H., J. A. Curry, and V. I. Khvorostyanov, 2005: A new double-moment microphysics parameterization for application in cloud and climate models. Part I: Description. *J. Atmos. Sci.*, **62**, 1665–1677, doi:10.1175/JAS3446.1.

Oye, R., C. Mueller, and S. Smith, 1995: Software for radar translation, visualization, editing, and interpolation. Preprints, *27th Conf. on Radar Meteorology*, Vail, CO, Amer. Meteor. Soc., 359–361.

Peterson, W. A., and Coauthors, 2005: The UAH-NSSTC/WHNT ARMOR C-band dual-polarimetric radar: A unique collaboration in research, education and technology transfer. Preprints, *32nd Conf. on Radar Meteorology*, Albuquerque, NM, Amer. Meteor. Soc., 12R.4. [Available online at https://ams.confex.com/ams/32Rad11Meso/techprogram/paper_96524.htm].

Potvin, C. K., D. Betten, L. J. Wicker, K. L. Elmore, and M. I. Biggerstaff, 2012a: 3DVAR versus traditional dual-Doppler wind retrievals of a simulated supercell thunderstorm. *Mon. Wea. Rev.*, **140**, 3487–3494, doi:10.1175/MWR-D-12-00063.1.

——, L. J. Wicker, and A. Shapiro, 2012b: Assessing errors in variational dual-Doppler wind syntheses of supercell thunderstorms observed by storm-scale mobile radars. *J. Atmos. Oceanic Technol.*, **29**, 1009–1025, doi:10.1175/JTECH-D-11-00177.1.

Rabin, R. M., S. F. Corfidi, J. C. Brunner, and C. E. Hane, 2004: Detecting winds aloft from water vapor satellite imagery in the vicinity of storms. *Weather*, **59**, 251–257, doi:10.1256/wea.182.03.

Rotunno, R., and J. B. Klemp, 1982: The influence of the shear-induced pressure gradient on thunderstorm motion. *Mon. Wea. Rev.*, **110**, 136–151, doi:10.1175/1520-0493(1982)110<0136:TIOTSI>2.0.CO;2.

Schmit, T., and Coauthors, 2013: *Geostationary Operational Environmental Satellite (GOES)-14* super rapid scan operations to prepare for GOES-R. *J. Appl. Remote Sens.*, **7**, 073462, doi:10.1117/1.JRS.7.073462.

——, and Coauthors, 2015: Rapid refresh information of significant events: Preparing users for the next generation of geostationary operational satellites. *Bull. Amer. Meteor. Soc.*, **96**, 561–576, doi:10.1175/BAMS-D-13-00210.1.

Sieglaff, J. M., D. C. Hartung, W. F. Feltz, L. M. Cronce, and V. Lakshmanan, 2013: A satellite-based convective cloud object tracking and multipurpose data fusion tool with application to developing convection. *J. Atmos. Oceanic Technol.*, **30**, 510–525, doi:10.1175/JTECH-D-12-00114.1.

Skamarock, W. C., J. B. Klemp, J. Dudhia, D. O. Gill, D. M. Barker, W. Wang, and J. G. Powers, 2005: A description of the Advanced Research WRF version 2. NCAR Tech. Note NCAR/TN-468+STR, 88 pp., doi:10.5065/D6DZ069T.

SPC, 2015: SPC severe weather events archive. Storm Prediction Center, accessed 1 June–12 August 2015. [Available online at http://www.spc.noaa.gov/exper/archive/events/.]

Velden, C. S., C. M. Hayden, S. J. Nieman, W. P. Menzel, S. Wanzong, and J. S. Goerss, 1997: Upper-tropospheric winds derived from geostationary satellite water vapor observations. *Bull. Amer. Meteor. Soc.*, **78**, 173–195, doi:10.1175/1520-0477(1997)078<0173:UTWDFG>2.0.CO;2.

——, T. L. Olander, and S. Wanzong, 1998: The impact of multispectral *GOES-8* wind information on Atlantic tropical cyclone track forecasts in 1995. Part I: Dataset methodology, description,

and case analysis. *Mon. Wea. Rev.*, **126**, 1202–1218, doi:10.1175/1520-0493(1998)126<1202:TIOMGW>2.0.CO;2.

——, and Coauthors, 2005: Recent innovations in deriving tropospheric winds from meteorological satellites. *Bull. Amer. Meteor. Soc.*, **86**, 205–223, doi:10.1175/BAMS-86-2-205.

Walker, J. R., W. M. MacKenzie, Jr., J. R. Mecikalski, and C. P. Jewett, 2012: An enhanced geostationary satellite–based convective initiation algorithm for 0–2-h nowcasting with object tracking. *J. Appl. Meteor. Climatol.*, **51**, 1931–1949, doi:10.1175/JAMC-D-11-0246.1.

Weisman, M. L., and J. B. Klemp, 1982: The dependence of numerically simulated convective storms on vertical wind shear and buoyancy. *Mon. Wea. Rev.*, **110**, 504–520, doi:10.1175/1520-0493(1982)110<0504:TDONSC>2.0.CO;2.

——, and ——, 1984: The structure and classification of numerically simulated convective storms in directionally varying wind shears. *Mon. Wea. Rev.*, **112**, 2479–2498, doi:10.1175/1520-0493(1984)112<2479:TSACON>2.0.CO;2.

Wilson, J. W., Y. Feng, M. Chen, and R. D. Roberts, 2010: Nowcasting challenges during the Beijing Olympics: Successes, failures, and implications for future nowcasting systems. *Wea. Forecasting*, **25**, 1691–1714, doi:10.1175/2010WAF2222417.1.

Witt, A., and S. P. Nelson, 1991: The use of single-Doppler radar for estimating maximum hailstone size. *J. Appl. Meteor.*, **30**, 425–431, doi:10.1175/1520-0450(1991)030<0425:TUOSDR>2.0.CO;2.

Wurman, J., J. Straka, E. Rasmussen, M. Randall, and A. Zahrai, 1997: Design and deployment of a portable, pencil-beam, pulsed, 3-cm Doppler radar. *J. Atmos. Oceanic Technol.*, **14**, 1502–1512, doi:10.1175/1520-0426(1997)014<1502:DADOAP>2.0.CO;2.